

*Sakari Pallaspuuro*

ON THE FACTORS  
AFFECTING THE DUCTILE-  
BRITTLE TRANSITION IN  
AS-QUENCHED FULLY AND  
PARTIALLY MARTENSITIC  
LOW-CARBON STEELS

UNIVERSITY OF OULU GRADUATE SCHOOL;  
UNIVERSITY OF OULU,  
FACULTY OF TECHNOLOGY





ACTA UNIVERSITATIS OULUENSIS  
C Technica 655

*SAKARI PALLASPURO*

**ON THE FACTORS AFFECTING  
THE DUCTILE-BRITTLE TRANSITION  
IN AS-QUENCHED FULLY AND  
PARTIALLY MARTENSITIC LOW-  
CARBON STEELS**

Academic dissertation to be presented, with the assent of the Doctoral Training Committee of Technology and Natural Sciences of the University of Oulu, for public defence in the Oulun Puhelin auditorium (L5), Linnanmaa, on 18 May 2018, at 12 noon

UNIVERSITY OF OULU, OULU 2018

Copyright © 2018  
Acta Univ. Oul. C 655, 2018

Supervised by  
Professor David Porter  
Professor Zhiliang Zhang

Reviewed by  
Doctor Jacques Besson  
Professor Kim Verbeken

Opponents  
Professor Bevis Hutchinson  
Professor Kim Verbeken

ISBN 978-952-62-1896-0 (Paperback)  
ISBN 978-952-62-1897-7 (PDF)

ISSN 0355-3213 (Printed)  
ISSN 1796-2226 (Online)

Cover Design  
Raimo Ahonen

JUVENES PRINT  
TAMPERE 2018

**Pallaspuro, Sakari, On the factors affecting the ductile-brittle transition in as-quenched fully and partially martensitic low-carbon steels.**

University of Oulu Graduate School; University of Oulu, Faculty of Technology

*Acta Univ. Oul. C 655, 2018*

University of Oulu, P.O. Box 8000, FI-90014 University of Oulu, Finland

***Abstract***

From the largest discontinuities to the smallest of the elements, various factors can threaten structural integrity. Susceptibility to these factors elevates with higher yield strengths. As-quenched low-carbon steels with a martensitic or martensitic-bainitic microstructure are modern ultra-high-strength structural steels. They can possess sufficient toughness, formability, and weldability, and are typically used in weight-critical and high-performance structures. Common problems with as-quenched steels with a yield strength of 900 MPa or more are that they do not obey the conventional correlation between the fracture toughness reference temperature  $T_0$  and the impact toughness transition temperature  $T_{28J}$  used in many standards and structural integrity assessment procedures, and a lack of design rules in general.

This thesis studies the relationship between the  $T_0$  and  $T_{28J}$  to provide additional knowledge for future standardisation, the microstructural features governing the toughness at these temperatures on both global and local scale, and whether hydrogen embrittlement is present at subzero temperatures. It uses steels produced via laboratory rolling and quenching as well as from pilot-scale and full-scale industrial production, studying them with standardised toughness tests, microstructural characterisation, fractography, and cohesive zone modelling.

As-quenched steels have a distinct correlation between  $T_0$  and  $T_{28J}$ . An improved general  $T_0 - T_{28J}$  correlation applies to a wide range of steels.  $T_{28J}$  correlates closely with a dynamic reference toughness, which can be used together with the fraction of detrimental  $\{100\}$  cleavage planes near the main fracture plain to effectively estimate the transition temperatures. On a local scale, centreline segregation decreases the effective coarse grain size, which more than compensates for the harmful effects associated with the higher hardness and inclusion content of the centreline, resulting in increased fracture toughness. Hydrogen embrittlement causes a decrease in fracture toughness and local deformability, thereby increasing  $T_0$  while leaving  $T_{28J}$  unaffected. Overall, the results show that high toughness demands good control of effective coarse grain size and hydrogen content.

**Keywords:** ductile-brittle transition, fracture toughness, grain size, hydrogen embrittlement, impact toughness, martensite, microstructure,  $T_0$ ,  $T_{28J}$



## **Pallaspuro, Sakari, Karkaistujen matalahiilisten martensiittisten ja osittain martensiittisten terästen transitiolämpötilaan vaikuttavista tekijöistä.**

Oulun yliopiston tutkijakoulu; Oulun yliopisto, Teknillinen tiedekunta

*Acta Univ. Oul. C 655, 2018*

Oulun yliopisto, PL 8000, 90014 Oulun yliopisto

### ***Tiivistelmä***

Tekijät suurimmista epäjatkuvuuskohdista aina pienimpään alkuaineeseen voivat uhata rakenteellista eheyttä, minkä lisäksi alttius näille kasvaa materiaalin myötölujuuden kasvaessa. Modernit karkaistun tilan ultralujat matalahiiliset rakenneteräkset voivat silti omata riittävän sitkeyden, muovattavuuden ja hitsattavuuden. Tyypillisiä käyttökohteita näille ovat painon suhteen kriittiset ja korkean suorituskyvyn rakenteet. Yleinen ongelma myötölujuudeltaan noin ja yli 900 MPa karkaistun tilan teräksillä on se, että ne eivät noudata perinteistä murtumissitkeyden referenssilämpötilan  $T_0$  ja iskusitkeyden transitiolämpötilan  $T_{28J}$  välistä korrelaatiota, jota käytetään useissa standardeissa ja suunnitteluohjeissa, jotka eivät myöskään vielä salli näin lujien terästen käyttöä.

Tämä väitöstyö tutkii transitiolämpötilojen  $T_0$  ja  $T_{28J}$  välistä suhdetta edistääkseen näiden terästen sisällyttämistä standardeihin, haurasmurtuma-sitkeyteen vaikuttavia mikrorakenteellisia tekijöitä sekä yleisellä että paikallisella tasolla, ja vetyhaurautta matalissa lämpötiloissa. Koeteräkset ovat laboratoriovalmisteisia, tuotantokokeita ja tuotantolaatuja. Niitä tutkitaan standardisoiduilla sitkeyskokeilla, mikrorakenteen karakterisoinnilla, fraktografialla ja koheesiovyöhykettä hyödyntävällä mallinnuksella.

Tulokset osoittavat karkaistun tilan terästen omaavan erityisen korrelaation  $T_0$  ja  $T_{28J}$  välillä. Muokattu, ultralujat teräkset huomioiva yleinen  $T_0 - T_{28J}$  -korrelaatio soveltuu laajalti eri terästyypeille.  $T_{28J}$  korreloi läheisesti dynaamisen referenssisitkeyden kanssa, jonka avulla yhdessä haitallisten {100} lohkomurtumatasojen osuuden kanssa voidaan estimoida joukko transitiolämpötiloja. Paikallisella tasolla keskilinjasuotauma pienentää efektiivistä karkeiden rakeiden kokoa, mikä suotauman suurista sulkeumista ja kovuudesta huolimatta parantaa murtumissitkeyttä. Vetyhauraus taas huonontaa sitkeyttä ja paikallista muodonmuutoskykyä myös matalissa lämpötiloissa nostaa  $T_0$  lämpötiloja. Kokonaisuutena erinomainen transitiolämpötilasitkeys vaatii efektiivisen karkeareakoon ja vetypitoisuuden minimointia.

*Asiasanat:* iskusitkeys, martensiitti, mikrorakenne, murtumissitkeys, raekoko, sitkehauraus transiatio,  $T_0$ ,  $T_{28J}$ , vetyhauraus



*To Alina, without whom this thesis might not exist, and  
to Akseli and Alda, without whom there would be so  
much less.*



## Acknowledgements

The work that I present in this thesis was carried out during the years 2012–2018 in various projects that dealt with the low-temperature toughness properties of ultra-high-strength steels both at the University of Oulu and the Norwegian University of Science and Technology, where I stayed for 6 months in 2015 and 2016–2018. The research work started in the Finnish Metals and Engineering Competence Cluster (FIMECC Ltd., later DIMECC Ltd.) programme Demanding Applications (DEMAPP, 2012–2014) and continued in Breakthrough Steels and Applications (BSA, 2014–2017).

The work received funding from the Finnish Funding Agency for Innovation (Tekes, currently Business Finland) under the FIMECC programmes, SSAB, Association of Finnish Steel and Metal Producers (Metallinjalostajien rahasto) and was supported by the Finnish foundation for technology promotion (TES), Jenny and Antti Wihuri foundation and the University of Oulu Graduate School. In addition, SSAB Europe Oyj provided the experimental materials. I am grateful for all this support.

I am very grateful for all the guidance and support that I received during the process from several experts and other people. I thank my supervisors Professor David Porter and Professor Zhiliang for all their invaluable guidance, comments, and support while staying at the both universities. Professor Jukka Kömi I thank for his long-standing support for my research projects during the years both within the industry and at the University of Oulu. To my doctoral training committee, Professor Timo Fabritius, Dr. Olli Nousiainen and Dr. Pasi Suikkanen, thank you. From the beginning of my journey into the field of materials science, I thank Professor Emeritus Pentti Karjalainen and Prof. Jouko Leinonen for all the inspiring lectures during my studies aiming for the Master of Science degree. Respective thanks to Dr. Mahesh Somani, and Mr. Ilpo Alasaarela and Mr. Tun Tun Nyo for their theoretical and practical help.

Furthermore, I thank my colleagues at the Materials and Process Engineering research group. Prof. Kim Wallin, Dr. Pasi Suikkanen, Dr. Saara Mehtonen, Dr. Anna Kisko, Dr. Antti Kaijalainen and Dr. Haiyang Yu, thank you for the fruitful collaboration and all the constructive discussions.

I am grateful for the whole Department of Structural engineering and all the people in the Nanomechanical lab for hosting me at the NTNU for such a long time. The experience is unforgettable. 大姐姐 Jianying, Sigurd, Senbo, the ladies of

2-48, Skibuddies and KT... you are too numerous to be named all, for all the scientific and non-scientific adventures – takk for turen!

For my friends, thank you for being there and everywhere during all these years. Special thanks belong to my parents Esa and Leila as well as to sister Elina and grandparents, but also for parents-in-law Lea and Veikko, for your endless support, trust, and encouragement that I and we have gotten from you.

Finally, I thank my dearest Alina, Akseli and Alda. I do not have enough words that could compensate for every moment that I get to spend with you, that could describe what you mean to me, nor do I have the time because I should already be there with you.

Trondheim, January 2018

Sakari Pallaspuuro

## Abbreviations

A	Area or total elongation
a	Crack length
ATM	Autotempered (lath) martensite
B	Specimen thickness
B <sub>0</sub>	Normalising thickness = 25.4 mm
b	Ligament size
c, c <sub>i</sub>	Constant
c <sub>YS</sub>	Yield strength related coefficient
C <sub>I</sub>	Initial hydrogen concentration
C <sub>L</sub>	Lattice hydrogen, also diffusible hydrogen
C <sub>V</sub>	Absorbed energy in Charpy-V test
C <sub>V-MIN</sub>	Minimum absorbed energy
C <sub>V-US</sub>	Upper shelf energy
C <sub>VB-US</sub>	Upper shelf energy equivalent to B mm thick specimen
C <sub>V10-US</sub>	Upper shelf energy equivalent to 10 mm thick specimen
CMOD	Crack mouth opening displacement
CT	Compact tension specimen
CVN	Charpy-V notch (test)
CZM	Cohesive zone modelling
d	Grain size or diameter
D <sub>eff</sub>	Effective diffusion coefficient
d <sub>eff</sub>	Effective grain size
d <sub>ecgs</sub>	Effective coarse grain size
d <sub>80%</sub>	Effective coarse grain size at 80% of the cumulative probability
d <sub>80%-i</sub>	Inclusion-d <sub>80%</sub>
d <sub>90%</sub>	Effective coarse grain size at 90% of the cumulative probability
d <sub>v</sub>	Volume-weighted average grain size
DBTT	Ductile-to-brittle transition temperature
DQ	Direct-quenched
E	Modulus of elasticity
EBSD	Electron backscatter diffraction
ECD	Equivalent circle diameter
EDS	Electron-dispersive spectrometer
EPMA	Electron probe microanalyser
FATT <sub>50%</sub>	Fracture appearance transition temperature
FRT	Finish rolling temperature

FT	Fracture toughness (test)
GB	Granular bainite
H	Hydrogen
HDL	Hydrogen degradation law
HE	Hydrogen embrittlement
HTT	High-temperature tempering
HV	Vicker's hardness
HV <sub>M</sub>	Hardness of martensite
K	Fracture toughness, stress intensity
K <sub>I</sub>	Stress intensity factor in mode I
K <sub>Id,ref</sub>	Dynamic reference toughness
K <sub>Jc</sub>	Elastic-plastic fracture toughness
K <sub>JC(1T)</sub>	Thickness-corrected elastic-plastic fracture toughness
K <sub>MED</sub>	Median fracture toughness
K <sub>MIN</sub>	Lower limiting fracture toughness
K <sub>0</sub>	Normalising fracture toughness corresponding to 63.2% cumulative failure probability
KAM	Kernel average misorientation
L	Longitudinal
L-T	Longitudinal-transverse
LB	Lower bainite
LOM	Light optical microscope
LCF	Laser confocal microscope
LTT	Low-temperature tempering
m	Exponent
OES	Optical emission spectrometer
P	Probability
P <sub>f</sub>	Cumulative failure probability
PAG	Prior austenite grain
Q&T	Quenched and tempered
R	Gas constant
R <sub>TOT</sub>	Total rolling reduction of PAG below T <sub>NR</sub>
R <sup>2</sup>	Coefficient of determination
R <sup>2</sup> <sub>adj.</sub>	Coefficient of determination adjusted for the number of predictors
RMSE	Root-mean-square error
RQ	Reheated and quenched
SEM	Scanning electron microscope
SENB	Single edge notched bend specimen

T	Temperature or transverse tensile specimen orientation
t	Thickness
T <sub>NR</sub>	Non-recrystallisation temperature
T <sub>T</sub>	Transition temperature
T <sub>Z</sub>	Absolute zero temperature
T <sub>0</sub>	Fracture toughness reference temperature
T <sub>0Q</sub>	Provisional reference temperature
T <sub>27J</sub>	27 J Charpy-V impact toughness transition temperature
T <sub>28J</sub>	28 J Charpy-V impact toughness transition temperature
T <sub>50</sub>	Temperature at the middle point of the transition curve
T <sub>FATT50%</sub>	Charpy-V 50% fracture appearance transition temperature
T-L	Transverse-longitudinal
TMCP	Thermomechanically controlled rolling process
TSL	Traction-separation law
UB	Upper bainite
UHSS	Ultra-high-strength steel
V <sub>H</sub>	Partial molar volume of hydrogen
V <sub>R</sub>	Cooling rate
XRD	X-ray diffraction
$\alpha$	Ferrite
$\gamma$	Austenite
$\gamma_{\text{eff}}$	Effective surface energy
$\gamma_{\text{ret}}$	Retained austenite
$\delta$	Separation of a cohesive element
$\delta_c$	Critical cohesive separation
$\zeta$	Viscosity parameter
$\sigma$	Standard deviation
$\sigma_c$	Critical cohesive stress
$\sigma_{c,H=0}$	Hydrogen-free critical cohesive stress
$\sigma_{d,\text{ref}}$	Dynamic reference strength
$\sigma_f$	Fracture stress
$\sigma_h$	Hydrostatic stress
$\sigma_{YS}$	Yield strength
$\sigma_{TS}$	Tensile strength
$\sigma_v$	Viscosity regulated cohesive stress
$\nu$	Poisson's ratio



## List of original research articles

This thesis is based on the following publications, which are referred throughout the text by their Roman numerals (I–V):

- I Pallaspuuro S, Linnell T, Suikkanen P, Porter D (2014)  $T_0 - T_{28J}$  correlation of low-carbon ultra-high-strength quenched steels, *Procedia Materials Science* 3: 1032–1037.
- II Wallin K, Pallaspuuro S, Valkonen I, Karjalainen-Roikonen P, Suikkanen P (2015) Fracture properties of high performance steels and their welds, *Engineering Fracture Mechanics* 135: 219–231.
- III Pallaspuuro S, Kaijalainen A, Mehtonen S, Kömi J, Zhang Z, Porter D (2018) Effect of microstructure on the impact toughness transition temperature of direct-quenched steels, *Materials Science and Engineering: A* 712: 671–680.
- IV Pallaspuuro S, Mehtonen S, Kömi J, Zhang Z, Porter D (2018) Effects of inclusions and local grain size on the low-temperature toughness of a low-carbon as-quenched steel, manuscript.
- V Pallaspuuro S, Yu H, Kisko A, Porter D, Zhang Z (2017) Fracture toughness of hydrogen charged as-quenched ultra-high-strength steels at low temperatures, *Materials Science and Engineering: A* 688: 190–201.

Sakari Pallaspuuro is the main and corresponding author of the publications I and III–V. He prepared the research plan, conducted the literature reviews, produced all the laboratory made materials, and planned the experiments. He made the characterisation and fractography, the data analysis together with co-authors, both statistical and finite element modelling, and wrote the manuscripts. He also did the mechanical testing for Paper V.

Exceptions to the above list are the older factory-made materials for I, II and III, for which he got the experimental raw data, bulk chemical compositions, microstructural characterisation for Paper III, EPMA and XRD analyses and inclusion mappings for Paper IV, and melt-extractions for Paper V.

For Paper II he provided the majority of the analysed UHSS data, commented, and co-authored the manuscript.

For Paper I, Teijo Linnell provided the factory-made raw data and test results, and Pasi Suikkanen commented on it. Antti Kaijalainen did the microstructural characterisation for Paper III. Saara Mehtonen and Jukka Kömi commented the manuscripts III and IV. For Paper V, Haiyang Yu helped with the modelling framework, and Anna Kisko did part of the EBSD measurements. Zhiliang Zhang commented on the contents of Papers III–V and David Porter of Papers I and III–V.



# Table of contents

Abstract	
Tiivistelmä	
Acknowledgements	9
Abbreviations	11
List of original research articles	15
Table of contents	17
<b>1 Introduction</b>	<b>19</b>
1.1 Background	19
1.2 Aims of the research	21
<b>2 Theoretical foundation</b>	<b>25</b>
2.1 As-quenched steels and their microstructure	25
2.2 Ductile-brittle transition	28
2.2.1 Impact toughness transition temperature $T_{28J}$	29
2.2.2 Fracture toughness and the reference temperature $T_0$	30
2.2.3 $T_0 - T_{28J}$ correlation	32
2.3 Microstructural features governing the toughness properties	34
2.4 Hydrogen embrittlement	37
<b>3 Experiments and modelling</b>	<b>41</b>
3.1 Materials	41
3.2 Methods	44
3.2.1 Mechanical testing	44
3.2.2 Characterisation and statistical analyses	45
3.2.3 Modelling of hydrogen embrittlement	47
<b>4 Results</b>	<b>49</b>
4.1 $T_0 - T_{28J}$ correlation of as-quenched steels	49
4.2 Microstructural factors governing the transition temperature toughness	53
4.3 Hydrogen embrittlement at low temperatures	61
<b>5 Discussion</b>	<b>63</b>
5.1 On the $T_0 - T_{28J}$ correlation	63
5.2 On the microstructural features	66
5.3 On the hydrogen embrittlement	70
5.4 Recommendations for further research	72
<b>6 Summary and conclusions</b>	<b>75</b>
<b>7 Novel features</b>	<b>79</b>
References	81
Original research articles	93



# 1 Introduction

## 1.1 Background

In today's world of ever-growing need for improved efficiency and reduced carbon dioxide (CO<sub>2</sub>) emissions, choice of material and its use are one key factor to consider. Steel is the second most used structural material, after cement-based concrete, with an annual global production of 1 620 million tonnes of crude steel in 2016 [1]. CO<sub>2</sub> is for the moment still an inevitable by-product of steel production, as per every tonne of steel the CO<sub>2</sub> emissions can be approximately 1.2 to 2.6 times that [2,3]. On the future end of the spectrum, for example the Swedish industry has stated that they are aiming for CO<sub>2</sub>-free steel production with demonstration plant trials targeted for 2025–2035 [4].

Utilisation is another matter, however. To maximise the customer value and to guarantee the safety, the requirements for design are constantly evolving and becoming increasingly complicated. The traditional simplistic approach to structural design and materials selection can consider just the strength of the materials; based on the anticipated stresses in the structure, a material with adequate strength and material thickness is chosen. A safety margin is implemented by choosing a material with higher strength, ductility, and/or larger thickness. Unfortunately, real life structures always contain flaws, which, in conjunction with the growing need for thinner and more efficient structures, demand more advanced dimensioning procedures.

Fracture toughness describes the material's ability to resist fracture, and fracture mechanics provides the tools to design against failure by quantifying the critical combinations of the applied stress, flaw size, and toughness. Brittle fracture is especially hazardous, as it often happens suddenly and unexpectedly. This thesis uses fracture mechanics to study the microstructural and mechanical material properties that influence the proneness to brittle fracture of a special class of ultra-high strength structural steels.

Structural steels are the most extensively used category of steel. They have standardised mechanical properties and chemical compositions, and can be used in applications whose design is guided by standards and structural integrity assessment procedures such as the European Eurocode 3 [5].

As-quenched low-carbon steels are a modern type of ultra-high-strength steels (UHSS, yield strength  $\sigma_{YS} \geq 900$  MPa) intended for structural use. These steels are

typically produced via thermomechanical rolling and direct quenching to a martensitic or martensitic-bainitic microstructure [6]. Produced with low carbon contents and optimized process parameters, the direct-quenched (DQ) steels are used in an untempered condition that still possesses a good combination of high strength and sufficient toughness, weldability, and formability. Typical applications are weight-critical and high-performance structures, like roof trusses, containers, booms, and other structural members of equipment for transportation and mobile lifting. They are a lower-cost alternative to conventional quenched and tempered (Q&T) UHSS: the savings come from leaner alloying, the avoidance of reheating before quenching, and the omission of additional tempering process after the quenching. The pursuit to use these high-performance materials can be justified with overall cost-effectiveness by maximising the load bearing capacity with minimal self-weight, for instance considering the maximum weight limits for road-going vehicles in the EU [7].

However, Nevasmaa et al. [8] and Kaijalainen et al. [9] showed with DQ steels that as-quenched ultra-high-strength DQ steels do not obey the conventional form of the correlation between the fracture toughness reference temperature  $T_0$  [10] and the 28 J Charpy-V impact toughness transition temperature  $T_{28J}$ , which was originally introduced by Wallin [11].  $T_0$  is the temperature where the median fracture toughness is  $100 \text{ MPa}\sqrt{\text{m}}$  for a 1-inch thick specimen. This correlation is presently used in European standardisation [12] and in the structural integrity assessment procedures of SINTAP [13] and FITNET [14]. The estimated  $T_0$  for DQ steels are well on the non-conservative side [8,9], so research is needed to evaluate their low-temperature toughness properties to assist their implementation in updated future standards.

The Master Curve method (MC) [15], a special case of the local approach to fracture [16,17], is the basis for the determination of  $T_0$  as per ASTM E1921 [10]. It combines a theoretical description of the scatter in the test data, a statistical size effect considering the stress triaxiality and sampling of the weakest link in the stressed area, and an empirically found temperature dependence of fracture toughness, to describe the fracture toughness in the brittle failure region.

Common to Eurocode 3 [5,12,18] and ASTM E1921 [10] is that they do not cover steels with yield strengths up to the regime of ultra-high-strength steels. In addition to this, very few studies are made concerning the validity of the MC, its temperature dependency [15], and of the conventional  $T_0 - T_{28J}$  correlation to UHSS [8,9,19]. The latest addition to Eurocode 3, EN 1993-1-12 [12], covers steels up to 700 MPa, and ASTM E1921 states that it is valid up to 825 MPa. A single

exception to these is the application-specific crane standard EN 13001-3-1 [20] which permits the use of steels with yield strength up to 1300 MPa. The clear lack of design rules limits the current structural application of UHSS.

To understand the applicability of UHSS better, one needs to take a deeper look at their fracture mechanical behaviour. Chemical composition and microstructure-based  $T_{28J}$  estimation still strongly relies on the pioneering work of Pickering and Gladman [21] and Mintz et al. [22], who worked with ferritic-pearlitic steels. Like the above description and estimation of fracture toughness, the UHSSs with their microstructures differing from ferrite and pearlite still need to be studied in detail. By studying the local features associated with brittle fracture initiation, one can identify the weakest microstructural links, and hopefully then find processing routes to eradicate, or at least, mitigate them.

Hydrogen has been known to reduce the ductility of steel for almost one and a half centuries [23], but even now in 2018 it is still under hot debate about how it actually does that [24]. The consequence of hydrogen embrittlement (HE) in the presence of a sufficient hydrogen content is the degradation of the mechanical properties of normally ductile/tough material, usually leading to a brittle failure by a time-dependent and thermally activated process. Higher strength increases the susceptibility to HE, and the level of degradation is dependent on the hydrogen concentration, stress level, and microstructure.

Due to the nature of hydrogen embrittlement, the studies are strongly limited to slow strain rates, tensile tests, and temperatures around room temperature. To the best knowledge of the author, only one other study has afterwards addressed the temperatures below zero degrees Celsius [25]. This leaves a research gap to be filled – i.e. to what degree is hydrogen embrittlement present at sub-zero temperatures, can it affect the toughness properties in standardised toughness tests, and if it does, to what extent does it contribute to the  $T_0 - T_{28J}$  correlation.

## 1.2 Aims of the research

The motivation for this thesis lies in the anomalous  $T_0 - T_{28J}$  correlation, the lack of standardisation for UHSS, and the insufficient knowledge regarding the microstructural factors governing the toughness properties of these steels. The main research questions are as follows:

- *Toughness correlation*: What kind of  $T_0 - T_{28J}$  correlation applies for as-quenched low-carbon UHSS and hardened welds?

- *Engineering application*: How can DQ UHSSs be implemented into design standards?
- *Description of impact toughness*: What are the factors controlling ductile-brittle transition temperatures determined on the bulk level, and what are their quantitative effects?
- *Description of fracture toughness*: What are the local factors governing brittle fracture initiation?
- *Low-temperature hydrogen embrittlement*: Does it exist? Can it affect the standard toughness properties at sub-zero temperatures?

To answer these questions, Papers I and II focus on the structural integrity assessment and the  $T_0 - T_{28J}$  correlation. Paper I tests the applicability of current correlations and deploys a best-fit approach to describe the correlation as a material-specific property based on results from 39 low-carbon as-quenched UHSSs.

Paper II discusses the usability of the Master Curve method focusing on novel direct-quenched UHSS and the materials of Paper I. Emphasis is on the  $T_0 - T_{28J}$  correlation and the temperature dependence. The paper proposes improvements to the method and establishes a general  $T_0 - T_{28J}$  correlation covering ferritic steels regardless of strength or quality.

Paper III investigates the quantitative effects of microstructure on the impact toughness transition temperature with 18 UHSSs with varying martensite and bainite contents. It proposes a new stress intensity parameter which, together with a crystallographic parameter, correlates closely with  $T_{28J}$ . The paper shows that a model consisting of these two parameters can effectively estimate a range of toughness transition temperatures.

Paper IV studies the local features that can cause the failure in a homogeneous “clean” material and a heterogeneous “dirty” material. Both large grains and large inclusions prove to be the dominant factors governing the fracture toughness. Fractographic evidence shows that the effective coarse grain size established in Paper III is able to describe the size of the brittle fracture initiators in both materials.

Paper V explores the effect of hydrogen on the fracture toughness and impact toughness of UHSS at sub-zero temperatures in the ductile-brittle transition temperature region. It uses tests with hydrogen-charged specimens, fractography, kernel-average misorientation measurements and cohesive zone modelling to analyse the results. It shows that hydrogen embrittlement is present at sub-zero

temperatures and that it causes an increase in the fracture toughness reference temperature  $T_0$ .

To best serve the aims of the thesis, I take the liberty to also include previously unpublished work that complements the above papers.

The thesis divides into three topics: the  $T_0 - T_{28J}$  correlation, microstructural properties, and hydrogen embrittlement. Section 2 contains the theoretical foundations giving a brief insight into the state of the art. Section 3 describes the materials and methods used to acquire the main results presented in Section 4. The discussion joins the analysis within the three topics in Section 5. Section 6 presents the overall conclusions, and Section 7 declares the novel features of the thesis.



## 2 Theoretical foundation

### 2.1 As-quenched steels and their microstructure

Generally, in hot-rolling a thick cast steel slab is first reheated in a furnace to high temperatures, typically over 1100 °C, to make the slab soft and deformable. Next, the reheated slab is rough rolled to a smaller thickness and desired width while keeping the slab in the temperatures above 1000 °C. After roughing the plate or strip is hot-rolled to its final thickness in consecutive rolling passes. The final passes are done preferably either at temperatures above the full-recrystallisation temperature, where new austenite grains nucleate thus refining the grain size, or below the recrystallisation-stop temperature, where the deformed austenite grains stay elongated. The non-recrystallisation temperature ( $T_{NR}$ ) that falls between these two temperatures is usually used in design over more appropriate recrystallisation-stop temperature, because it is easier to define and more widely available in the literature. After the final pass, the steel plate or strip is either left to cool in air or actively cooled to achieve desired microstructures. [6]

Accelerated on-line cooling of the hot-rolled plates was first developed in Japan in 1979 and it was adopted to production in Japan and Europe in the 1980s [26]. In the case of high-strength ferritic-bainitic low-alloyed steels, the combination of a thermomechanically controlled rolling process (TMCP) and fast cooling improved strength, toughness, and weldability as a result of the fact that carbon content and grain size could be reduced. Further increased cooling rates facilitated direct quenching of steel strips to a martensitic or martensitic-bainitic microstructure to produce ultra-high-strength steels [27,28].

For a given strength level, DQ steels differ from the Q&T steels produced on plate mills in their microstructure and level of alloying. Furthermore, DQ steels can be produced on both plate and strip mills, which allows further grain refinement with shorter inter-pass times and flexibility with product sizes and thicknesses [6]. While both can have lath-martensitic microstructure, DQ steels can contain various amounts of lower bainite, upper bainite and granular bainite too. With fully martensitic microstructures, the steels differ in the carbide size and structure [29], dislocation density which decreases with recrystallisation in reheating and recovery in tempering [29,30], residual stresses formed in quenching and relieved in tempering [31–33], and in possible differences in the hydrogen contents and sensitivities to it [34–36].

The lath-martensite in DQ steels is partially autotempered due to the low carbon content and relatively high start temperature of martensite transformation. In autotempering, carbon segregates to near dislocations and lath boundaries [37], either forming very fine and homogeneously distributed transition carbides and lath-like cementite ( $\text{Fe}_3\text{C}$ ) [29,30] or residing in the inter-lath residual austenite film [38,39]. In Q&T steels, the carbides are enlarged, more spheroidal cementite and alloy carbides [29,30].

In low-carbon steels ( $\leq 0.30$  wt.% C), martensite forms from the parent austenite in sufficiently rapid cooling by ideally diffusionless transformation. This low-carbon martensite is susceptible to carbon diffusion during the rest of the cooling resulting in an autotempered body-centred cubic (bcc) crystal structure [29,37]. Figure 1 presents the structure of lath-martensite in its complex, hierarchical, and heterogeneous nature. A prior austenite grain consists of packets, blocks, sub-blocks and laths [40]. Between the laths, thin films of residual austenite ( $\gamma_{\text{ret}}$ ) can be found [38,39] which can play an important role on the local deformation capability of martensite [41]. On the other hand, Hutchinson et al. [33] showed that local residual compressive stresses that form in the martensitic transformation can explain the yielding behaviour of martensitic steel. The possible “coarse laths” are the ones that have been formed earliest in the martensitic transformation, which makes them more autotempered and therefore softer than their surroundings [39,42].

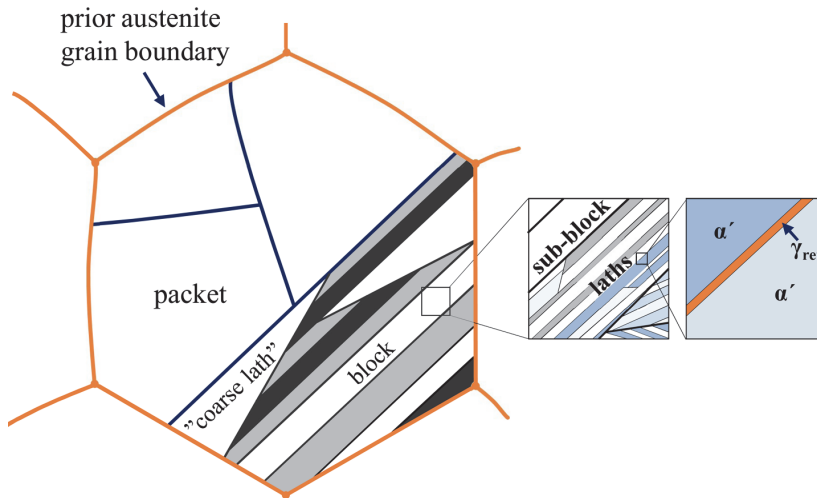


**Fig. 1. The schematic structure of as-quenched lath martensite according to Morito et al. [40] and Morsdorf et al. [39].**

Considering Kurdjumov-Sachs (K-S) orientation relationships, there are 24 possible crystallographic variants between martensite and a parent austenite. These group into four possible packets of distinct parallel  $\{110\}_\alpha$  planes that each have six possible variants of distinct parallel directions. A packet can consist of three distinct blocks (or Bain variants), which are further sub-divided into two sub-blocks formed of laths. The smallest ferritic units, laths, can be considered as highly dislocated bcc crystals that all have the same  $\{111\}_\gamma$  habit plane in the parent austenite grain. Laths and sub-blocks are separated by low-angle grain boundaries that have a misorientation of less than  $5^\circ$  and around  $10.5^\circ$ , respectively. Block and packet boundaries are high-angle boundaries with a misorientation of at least  $15^\circ$ . [40,43]

If the cooling rate and/or the hardenability of the material is insufficient to produce a virtually fully martensitic microstructure, several bainite morphologies are the next to appear, forming above the temperatures of the martensitic transformation. Going upwards on the temperature scale, the order of formation is: lower bainite (LB), upper bainite (UB), and granular bainite (GB) [30].

LB consists of lath-like ferrite with cementite embedded inside the laths or in contact with the lath boundaries. Characteristic to it, the cementite particles have their long axis inclined at approximately  $60^\circ$  to the growth direction of the ferrite laths [44]. UB has a lath-like morphology too, but the laths are elongated and

ordered in packets. Carbon distributes along the lath boundaries forming elongated cementite particles in UB. GB consists of coarse granular-like ferritic plates with islands of retained austenite and some high-carbon martensite. A typical feature of GB is the lack of carbides in the microstructure, whereas in microalloyed steels LB and UB can contain fine alloy carbides also within the laths. The sub-grain structure of GB is coarser than those of LB and UB [45,46], and in general, bainitic morphologies formed at higher temperatures contain more low-angle boundaries [47,48].

## 2.2 Ductile-brittle transition

An ideal pure material can fail by a complete necking of a stressed cross-section. In engineering materials, plastic flow will be followed by ductile crack growth via microvoid initiation, void growth, and coalescence of these microvoids. A void forms typically at an inclusion or other second-phase particle, either by interface decohesion or cracking of a particle. The void grows under sufficient plastic strain and hydrostatic stress. When two or more voids are close enough to each other, localising stresses and strains cause them to interact, which leads to necking between the voids and their coalescence – causing the crack to grow. [49]

When the deformation capability of a ferritic steel decreases, usually by lowering temperature, they experience a transition from ductile to brittle, where brief plastic flow and ductile crack growth are eventually followed by an increasing amount of brittle crack growth by cleavage. In the ductile-brittle transition region, between the expectedly ductile upper shelf and the completely brittle lower shelf, ductile and brittle mechanisms will alternate due to local cleavage crack arrests where the crack driving force drops too low. The probability for brittle failure increases as more material is sampled during the crack growth before the critically sized microcrack is encountered that can cause a global failure. [49]

Cleavage occurs in bcc materials as a rapid transgranular crack propagation along the crystallographic  $\{100\}$  planes that are the easiest to debond. In order to initiate it, a local (microstructural) discontinuity ahead of the macroscopic crack tip must provide sufficient stress concentration for the bond strength to be exceeded. A simple method to assess the acuity of microstructural features is to treat them as Griffith cracks, Eq. (1), where fracture stress  $\sigma_f$  is a function of the approximated stress concentration factor  $c$ , the modulus of elasticity  $E$ , the effective surface energy  $\gamma_{\text{eff}}$ , the diameter of the discontinuity  $d$ , and the Poisson's ratio  $\nu$ . For a penny-shaped crack ahead of a macroscopic crack tip, which is a feasible

approximation for many microstructural features that can be described with an equivalent circle diameter (ECD),  $c = \pi$ .

$$\sigma_f \text{ [MPa]} = \sqrt{c \times \frac{E\gamma_{eff}}{(1-\nu^2)d}} = \sqrt{\frac{\pi E\gamma_{eff}}{(1-\nu^2)d}} \quad (1)$$

### **2.2.1 Impact toughness transition temperature $T_{28J}$**

The Charpy impact test is the most commonly used standard test method to measure the toughness of the materials (ASTM E23 [50], EN 10045-1 [51] and ISO 148-1 [52]). In the test, a pendulum is dropped towards the specimen to break it. The energy that the material absorbs in the test is calculated from the difference between the start and end angles of the swing with the known striker mass and pendulum arm length. The default specimen type has a V-notch and dimensions of 10×10×55 mm (Charpy-V impact test, CVN), but sub-sized specimens with reduced thickness are also common.

Determinable factors from a single specimen are total impact energy, fracture appearance and lateral expansion. Further instrumentalisation of the test equipment allows the recording of the force signal as a function of time. Due to the inherent scatter in the toughness results, the data collected from multiple specimens is normally used to define toughness at a given temperature of interest or a certain ductile-brittle transition temperature value. Such commonly used values are  $T_{50}$ , which is the halfway point in the transition curve,  $FATT_{50}$ , which is the 50% ductile/brittle fracture appearance transition temperature or  $T_{27J}$  and  $T_{28J}$ , which are the temperatures on the transition curve that correspond to an energy level of 27 J and 28 J, respectively. This thesis will use  $T_{28J}$ , the French interpretation of the American 20 ft-lb, but it is only the philosophy of the rounding that differs, since all three transition temperatures are within 1 °C [19].

The benefits of  $T_{28J}$  are that it lies on the less scattered lower shelf side of the transition region, and as opposed to  $T_{50}$  or  $FATT_{50}$ , it does not necessarily rely on the determination of the full transition curve or the determination of subjective fracture appearance, respectively. An energy level of 27–28 J is also low enough to mostly omit the tearing resistance dependence of the sheared area. Furthermore,  $T_{28J}$  is important as it is chosen as the basis for the estimation of the fracture toughness reference temperature  $T_0$  [10], and it is commonly used as the minimum specified toughness for many steel grades.

An established way to treat the scatter-ridden test data is to utilise a least-square fit with a sigmoidal function. For CVN data, the most commonly used function is the hyperbolic tangent function, originally introduced by Oldfield [53]. Eq. (2) shows it in a simple form, where  $C_{V-US}$  is the upper shelf energy,  $C_{V-MIN}$  the minimum lower shelf energy (usually 2–7 J),  $T$  the given temperature,  $T_{50}$  the temperature at the middle point of the transition curve, and  $C$  the slope coefficient. An alternative to hyperbolic tanh function is an exponential function with the form of Eq. (3). If the material thickness is too thin for full-sized CVN specimens, Eq. (4) yields an estimate of the full-size equivalent upper shelf energy  $C_{V10-US}$  based on the upper shelf energy  $C_{VB-US}$  of the sub-sized specimens with a thickness of  $B$ , where factor  $c$  is either 1.00 or 1.09 [19].

$$C_V[J] = \frac{C_{V-US} - C_{V-MIN}}{2} \times \left( 1 + \tanh\left(\frac{T - T_{50}}{C}\right) \right) + C_{V-MIN} \quad (2)$$

$$C_V[J] = \frac{(C_{V-US} - C_{V-MIN}) \times \exp\left(\frac{2(T - T_{50})}{C}\right)}{1 + \exp\left(\frac{2(T - T_{50})}{C}\right)} + C_{V-MIN} \quad (3)$$

$$\frac{C_{VB-US} \times 10}{C_{V10-US} \times B} = c - \frac{0.5 \times \exp\left(\frac{2(C_{V10-US}/B - 44.7)}{17.3}\right)}{1 + \exp\left(\frac{2(C_{V10-US}/B - 44.7)}{17.3}\right)} \quad (4)$$

## 2.2.2 Fracture toughness and the reference temperature $T_0$

In fracture mechanics, a single parameter ( $K$ ,  $J$ , and CTOD) can characterise the crack-tip conditions under small-scale yielding, that is when the plasticity is confined to regions close to the crack tip when compared to the in-plane dimensions of the cracked body. This criterion is approximately valid if the specimen still maintains a high level of triaxiality, as in the case of edge-cracked specimen in bending [49].

The stress intensity factor  $K$  describes the crack-tip conditions and the toughness of a material under linear elastic conditions, i.e. when the material deforms proportionally to the load before an eventual structural brittle failure.  $K$  can be corrected for moderate crack-tip yielding, but eventually its validity will break down. Elastic-plastic fracture mechanics (EPFM) applies to materials and specimens that exhibit nonlinear behaviour. Under EPFM, the  $J$ -integral and CTOD (crack-tip-opening displacement) describe the crack tip conditions and can be used as fracture criteria. The  $J$ -integral can be regarded as both a stress intensity parameter [54,55] and an energy parameter that is equivalent to the energy release

rate in nonlinear elastic materials [56]. For further reading, Anderson [49] explains the fundamentals of fracture mechanics.

This thesis considers fracture mechanics from the point of view of the determination of quasi-static fracture toughness as  $K_{Jc}$ , elastic-plastic equivalent stress intensity factor derived from the J-integral at the point of brittle fracture initiation, according to the ASTM test standards E1820 [57] and E1921 [10]. In these, the J-integral is calculated by dividing it to an elastic and a plastic part. The elastic part is defined via the relation with  $K$ , and the plastic part is estimated from the plastic area under the load-displacement curve. The focus is on the determination of the fracture toughness reference temperature  $T_0$  (the test temperature where the median  $K_{Jc} = 100 \text{ MPa}\sqrt{\text{m}}$  for 1T sized (1 inch thick) specimens) as per ASTM E1921 [10], which has its basis in the Master Curve method [15].

Fig. 2 presents the principle of how the MC describes the fracture toughness in the brittle fracture region. Briefly, the theoretical part is based on statistical modelling of the cleavage fracture event and yields the fracture toughness as a function of specimen thickness ( $B / B_0$ ,  $B_0 = 25.4 \text{ mm}$ ) and median fracture toughness  $K_{MED}$ . For engineering purposes, this cumulative probability of failure  $P_f$  has the form of Eq. (5), where  $K_I$  is the stress intensity factor in Mode I (opening) loading,  $K_{MIN}$  is the minimum fracture toughness (here  $20 \text{ MPa}\sqrt{\text{m}}$  [10]),  $K_0$  is the normalising fracture toughness corresponding to cumulative failure probability of 63.2%, and  $m = 4$ . Eq. (6) expresses the relation between the median fracture toughness  $K_{MED}$  and  $K_0$ .  $K_{MIN}$  is the lower limiting stress intensity factor, below which the cleavage crack propagation is not expected in ferritic steels. The median  $K_{Jc}$  enable the description of scatter. The weakest link nature of the cleavage fracture initiation interlinks the scatter and the size-effect.

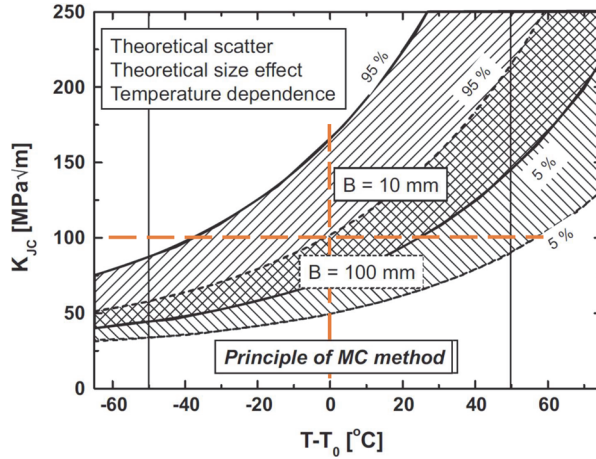


**Fig. 2. The principle of the Master Curve method after Ref. [15]. [Paper II, modified and reprinted by permission of Elsevier]**

$$P_f = 1 - \exp\left(-\frac{B}{B_0} \times \left(\frac{K_I - K_{MIN}}{K_0 - K_{MIN}}\right)^m\right) \quad (5)$$

$$K_{MED} [MPa\sqrt{m}] = 0.912 \times (K_0 - K_{MIN}) + K_{MIN} \quad (6)$$

Eq. (7) expresses the approximate temperature dependency of the fracture toughness  $K_0$  with a default  $c = 0.019$ . The dependency is empirical and bases on a best fit of data with  $T_0 = -109 \dots +51$  °C and  $\sigma_{YS} = 280 \dots 620$  MPa. Also, ASTM E1921 itself states that it covers ferritic steels only up to yield strength of 825 MPa. Note that Eq. (7) is valid only within  $T_0 \pm 50$  °C {ASTM E1921}, Fig. 2. For a complete description of the Master Curve method, the reader can turn to Wallin [19].

$$K_0 [MPa\sqrt{m}] \approx 31 + 77 \times \exp(c \times (T - T_0)) \quad (7)$$

### 2.2.3 $T_0 - T_{28J}$ correlation

Compared to the cheap, fast, and easy to perform Charpy impact toughness testing, standardised fracture toughness testing is expensive, time consuming, and more difficult to interpret. Testing becomes even more difficult with irradiated specimens from reactor pressure vessels and with the surveillance requirements for commercial nuclear power plants. These have encouraged many researchers, Refs. [11,58–62] for example, to attempt to correlate these together, often yielding

material and case dependent solutions. This thesis focuses on the few  $T_0 - T_{28J}$  correlations because they are the most relevant for the standardised use of UHSS in load-bearing structures.

The most important differences between a fracture toughness test (FT) and the Charpy-V impact toughness test in the brittle fracture region are the flaw geometry, the event described in the tests, and loading rate. FT has a deep sharp crack, whereas CVN has a shallow blunt notch. FT describes the fracture initiation, and the non-instrumentalised CVN contains both the initiation and propagation. Loading rate in FT is here quasi-static whereas in CVN it is dynamic. Both higher loading rate (CVN) and higher notch acuity (FT) decrease the toughness, but their combined differences seem to mostly cancel each other out [19]. As a change in  $\sigma_{YS}$  affects both parameters, the extent of the cancellation can be anomalous for UHSSs.

Marandet and Sanz were the first to relate the  $100 \text{ MPa}\sqrt{\text{m}}$  transition temperature to  $T_{28J}$  [60]. Wallin [11] included the effect of specimen thickness, but the correlation was still strongly limited to nuclear pressure vessel steels. His subsequently validated correlation, Eq. (8), is currently included in the Eurocode 3 [63] and in the structural integrity assessment procedures of SINTAP [13] and FITNET [14].

$$T_{0-Est.1}[\text{°C}] = T_{28J} - 18, \sigma \pm 15\text{°C} \quad (8)$$

However, steels with yield strengths of 900 MPa or more have not yet been sufficiently validated for the basic MC [15], the  $T_0 - T_{28J}$  correlation of Eq. (8) [11], or with regard to ASTM E1921 ( $\sigma_{YS} \leq 825 \text{ MPa}$ ) [10]. More recently, Wallin [19] developed an improved correlation, Eq. (9) that accounts for the effects of yield strength  $\sigma_{YS}$  and CVN upper shelf energy. This correlation is based on data that already includes some materials (~5%) that have a yield strength above 900 MPa. Higher applied  $\sigma_{YS}$  emphasises the question of how much the  $T_0 - T_{28J}$  correlation is affected by the yield strength and strain hardening exponent that relates to it. According to Wallin [19], yield strength has a nearly linear effect, and the upper shelf energy is significant mainly with low values below 100 J.  $C_{V-US}$  is apparently included into Eq. (9) because a very low upper shelf energy can over-suppress the tanh fitted  $T_{28J}$ .

$$T_{0-Est.2}[\text{°C}] \approx T_{28J} - 87 + \frac{\sigma_{YS}}{12} + \frac{1000}{C_{V-US}}, \sigma \pm 18\text{°C} \quad (9)$$

### 2.3 Microstructural features governing the toughness properties

The critical factors that can determine the toughness properties in the transition temperature region divide into three categories of discontinuities in the microstructure: 1) small particles, like carbides and carbide clusters [64–67], 2) larger inclusions and brittle second phase particles [68–74], and 3) grains [9,21,22,46,75–88]. These have been used to explain and estimate toughness properties, both interchangeably and often indirectly, and both at very low temperatures, where toughness is controlled by crack nucleation, and at the DBTT, where toughness is controlled by crack propagation [77]. The failure initiation is often a complicated interaction between large grains and large particles [89–91].

Of all the factors, toughness is mainly correlated to grain size and often with an inverse square root dependence [21,22,76,82,83,85,87]. Barr & Tipper [75] showed first with the Liberty ships that the DBTT was elevated with increasing ferrite grain size. Since then, various grain size definitions have been linked to toughness: ferrite grain size in ferritic-pearlitic steels [21,22], and in bainitic and martensitic steels the prior austenite grain size (PAG) [76,88], packet size [76,77,79] and block size [82]. More generally, it is the size of the grains separated by high-angle grain boundaries between the  $\{100\}$  planes that is important [9,46,78,80,81,83–85,87,88], Fig. 3. This effective grain size in martensitic and bainitic microstructures corresponds to blocks from different Bain variants [82,86,92] with a grain boundary misorientation of at least  $15^\circ$  [43,48].

Because an industrial material never has an exact grain size but rather a distribution of grain sizes, several definitions aim to provide a suitable description considering strength and toughness: average effective grain size  $d_{\text{eff}}$  [46,78,80,81,83], volume-weighted average grain size  $d_v$  (for strength) [93], and the size of the coarsest grains at various percentiles in the cumulative grain size distribution –  $d_{80\%}$  [85,87] and  $d_{90\%}$  [9,94,95]. Lehto et al. [93] described the strength of heterogeneous weld microstructures with a modified Hall-Petch equation using  $d_v$ , and it could be a viable option for toughness, too.

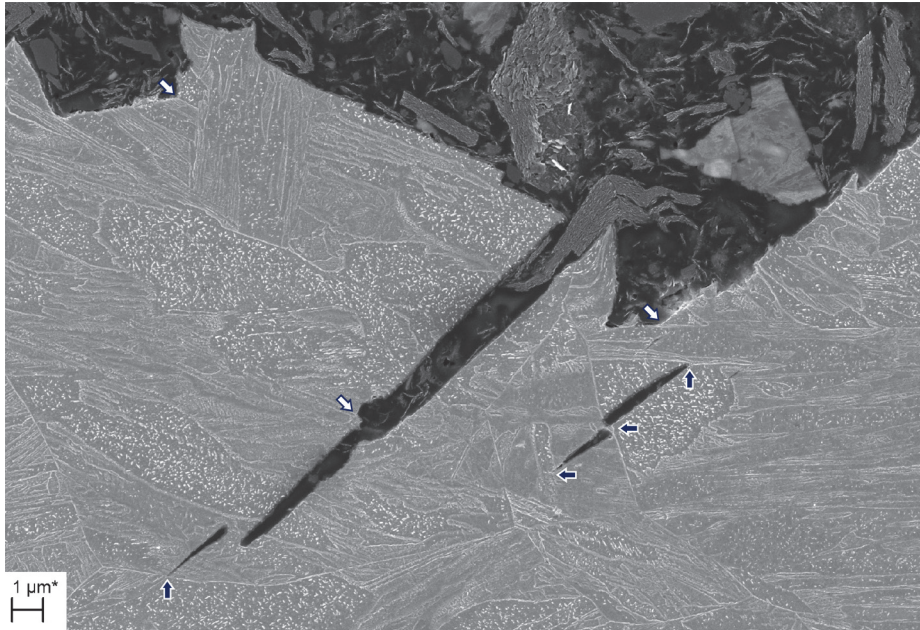


**Fig. 3. The crack path in a pre-cracked specimen tested at a sub-zero temperature highlights the importance of the high-angle grain boundaries. The dark arrows show these effective grain boundaries where the crack has arrested, and the light arrows point to some of the boundaries where the crack has deflected. [Paper V, modified and reprinted by permission of Elsevier]**

Untempered martensite is historically considered unwanted as being too brittle for structural use. However, modern low-carbon steels with as-quenched and partly martensitic microstructures can possess similar or even better low-temperature toughness properties than the conventional softer phases due to their finer effective grain size and the autotempering that results from the low carbon content, which leads to relatively high martensite start temperatures [37,46,80,81,87]. Successful methods to improve the DBTT of as-quenched steels are increasing the bainite content [9,46], refinement of the prior austenite grain structure [9,81,82], and these two methods combined by lowering the finish rolling temperature (FRT) below  $T_{NR}$  [9,81,95]. Granular bainite seems to have a harmful effect on toughness due to its coarse grain and sub-grain structures and M-A constituent islands [45,46]. Recent studies on ferritic and bainitic pipeline steels highlight the importance of texture, especially the fraction of deleterious  $\{100\}$  cleavage planes parallel to the fracture plane [96–99].

Many studies have been dedicated to deriving formulae to predict impact toughness transition temperatures. Pickering and Gladman [21] linked  $T_{50}$  to the inverse square root of the grain size of ferritic-pearlitic steels, and Mintz et al. [22] complemented the predictive model by including the detrimental factors of grain boundary carbides and elevated yield stress. Bhattacharjee et al. [78] incorporated effective grain size to the modified Mintz type equation for ferritic steels, and Gutiérrez [83] extended the equation to bainitic microstructures. Isasti et al. [85] added the detrimental effects of M-A islands and grain size heterogeneity. Pillot and Pacqueau [100] used an approach based on the Master Curve to define the CVN transition curve with just the yield strength and a CVN value in the transition range. These estimates show that, other factors being equal (except with Ref. [100]), elevated  $\sigma_{YS}$  reduces toughness.

Excessive macrosegregation during the solidification generally leads to impairment and anisotropy of mechanical properties due to local enrichment of impurities and hardening elements. Solid state diffusion is too slow to enable the homogenisation of macrosegregation in subsequent heat treatments, so the segregation persists through the process route affecting the austenite recrystallisation kinetics, grain growth, hardenability and the formation and growth of carbides. Macrosegregation can be pronounced at the centreline of continuously cast steel slabs, as it is the last to solidify and tends to contain detrimental larger Al, Ca, Mn and Ti based non-metallic inclusions [70–73,101]. On the other hand, the concentration of alloy elements can lead to the refinement of austenite grain size via solid solution effects on recrystallisation and grain growth and/or microalloy carbides and nitrides that can pin the grain boundaries [30]. The properties of the centreline of the final steel plate and the centreline segregation are important for toughness as up to 90% of the brittle failures originate in the middle third of the material thickness [102].

Cracks formed on the fracture surfaces parallel to the rolling plane and normal to the specimen crack plane are known as splitting (also delamination). Splitting is most often present in impact toughness specimens of thermomechanically rolled steels, associates sometimes to segregation and manifests local anisotropy of toughness [103–105]. Splits introduce an internal size effect into the test specimens making full-size specimens behave like joint sub-sized specimens by reducing the plane strain constraint, which in turn increases the proportional amount of shear lips.

Splitting can increase the absorbed energy in the DBTT region and so lower the resulting transition temperature [97,103,105–107]. This is due to the higher

fraction of shear lips that consume more energy than cleavage, and because splitting increases the absorbed impact energy by creating additional surfaces perpendicular to the main fracture plane [103,106]. Even though the new surfaces generated in splitting consume slightly less energy per unit area than the original ligament area, the generated splits toughen the material throughout the DBTT region [106]. On the other hand, splitting reduces the upper shelf energy [107] since crack propagation by ductile tearing absorbs about twice the energy of a fully shear fracture [19].

## 2.4 Hydrogen embrittlement

The detrimental effect of HE on mechanical properties is clear, but from several proposed mechanisms none have been fully accepted because experimental observations are linked to different mechanisms. This controversiality is at least partly due to the multitude of microstructural and environmental factors and loading properties. The two most cited models for HE are the hydrogen enhanced localised plasticity (HELP) and the hydrogen enhanced decohesion (HEDE) that both regard the failure criteria as a critical combination of hydrogen concentration, stress and strain, but differ in the details of the mechanisms. HELP is based on the observations that H increases dislocation mobility and hence increases plastic deformation ahead of the crack tip so that the fracture surfaces show localised plasticity while the behaviour remains macroscopically brittle [108,109]. On the other hand, HEDE is based on the hypothesis that H reduces the cohesive force between the metal atoms and so eases the separation of grain boundaries or cleavage planes [110]. Due to their nature, diffusible hydrogen is more relevant to HELP, but with high trap densities, such as in the case of martensitic steels, trapped hydrogen can become important with HEDE.

Hydrogen embrittlement is typically associated with intergranular fracture, quasi-cleavage, and “flat” features that are all observed in lath-martensitic steels [36,111–115]. Intergranular fracture propagates along prior austenite grain boundaries and is considered as brittle [116]. Quasi-cleavage is often misinterpreted as cleavage fracture or used to describe a combination of brittle and ductile features. As opposed to  $\{100\}$  cleavage cracks, it involves a cleavage-like crack initiating and propagating along  $\{110\}$  slip planes by the growth and coalescence of shallow voids that form between or in slip bands [117]. Very fine and highly deformed tear ridges separate the voids, often with lath-sized intervals [113] that separate quasi-cleavage further from cleavage with relevant size-scale of

a given effective grain size. Hydrogen-related local “flat” features follow PAG boundaries [118] and consist of undulating surfaces covered with nanoscale mounds with highly dislocated microstructure beneath the surfaces [113,114]. Similar features can also be transgranular and follow {110} slip planes [36]. Nagao et al. [113] first stated that hydrogen-related crack growth is due to a hydrogen-enhanced and plasticity-mediated decohesion mechanism. Most recently they concluded [24] that this mechanism is a coupled HEDE–HELP induced failure process, and that hydrogen-related intergranular cracking happens when dislocation pile-ups impinge on PAG boundaries, and that quasi-cleavage happens when the dislocation pile-ups impinge on block boundaries. The kernel average misorientation (KAM) method can qualitatively measure HE related deformation on and under the fracture surfaces [119,120], and could be a viable tool to distinguish the crack growth mechanisms. It does this by providing information about the local variations in lattice orientation, i.e. local plastic deformation.

The susceptibility to HE increases with increasing yield strength, hardness, and hydrostatic stress levels [112,121–125]. High hydrostatic tensile stress levels, residual stresses included, translate to larger lattice expansion and faster hydrogen diffusion into the stressed areas. “Cold cracking” can occur even without applied external stresses [34]. Local hydrogen concentration is the crucial factor, but how it forms also depends on diffusivity of hydrogen (regarding both absorption and desorption as a function of exposure history) and its solubility, which in turn are affected by the environmental factors, temperature, crystal structure, hydrogen trapping, and their history. Traps are local discontinuities of varying strength that can hold the hydrogen in place. Traps can be vacancies, dislocations, cavities, and various interfaces. Generally, only diffusible hydrogen is considered effective, but with very high trap density, trapped hydrogen should promote HEDE mechanism. As-quenched steels naturally combine both aspects of high stress levels and high trap density with dislocations, carbides, grain, and sub-grain boundaries.

The microstructural factors translate to hydrogen diffusivity, the effective diffusion coefficient, which follows a temperature dependent Arrhenius equation. A problem arises with respect to both diffusivity and HE in that HE measurements are lacking for temperatures below room temperature: only one study considers sub-zero temperatures [25] while others lower bound to the subsea-relevant temperature of +4 °C [122]. The reported experiments are mostly limited to relatively slow strain-rates. Wang et al. [112] found the degradation of the notch tensile strength of tempered martensite as a function of diffusible hydrogen to follow a power-law type of behaviour. Tvrđy et al. [123] reported the static

threshold toughness of UHSS to drop from 80 to around 20 MPa $\sqrt{m}$  in an 0.5M NaCl solution. Based on the 20% loss of total elongation, a linear relationship between tensile strength and critical hydrogen content was found for as-quenched and quenched and tempered steels in Refs. [124,125].

A promising method to simulate HE from a HEDE point of view is a hydrogen-informed three-step procedure including a cohesive zone modelling (CZM) step [126,127]. The three-step HE modelling procedure is an interesting option for studying the brittle fracture region with hydrogen and for interpreting and widening the predictions based on experiments. CZM provides a phenomenological representation of the fracture process with interfacial separation between the inserted cohesive elements on the anticipated crack path between the solid elements. A traction-separation law (TSL) describes the behaviour of the cohesive elements based on the calibration according to the experimental results. It is characterised by the cohesive strength ( $\sigma_c$ ), the cohesive separation ( $\delta_c$ ) and the area below  $\sigma - \delta$  curve that is the cohesive energy. The reader is referred to Ref. [128] for more details regarding CZM. The effects of HE on the mechanical response of the model can be incorporated into the CZM by using a fundamental hydrogen degradation law (HDL), which defines the decrease of  $\sigma_c$  as a function of the lattice hydrogen concentration. Yu et al. [129] recently calibrated a CZM-based uniform HDL to an engineering size scale from notched tensile tests with quenched and tempered AISI 4135 steel with microstructure relevant to this thesis. They observed excellent agreement between the simulations and test results with their HDL, which is applicable to all the specimen geometries thanks to successful normalisation. Furthermore, their HDL omits the questionable transferability to engineering components of a previously favoured HDL of Ref. [130], which is based on first principle simulation results.



## 3 Experiments and modelling

### 3.1 Materials

In total, this thesis consists of 68 different ultra-high-strength steels comprising laboratory cast, rolled and quenched materials, and steels from pilot-scale direct-quenching and normal production. Of the as-quenched (untempered) materials, 42 are direct-quenched (DQ) and 13 reheated and quenched (RQ). The microstructures are either martensitic or martensitic-bainitic. The martensite is mainly autotempered lath martensite and the bainitic constituents are lower or upper bainite. In addition, I present here 13 quenched and tempered steels (Q&T): 8 made by low-temperature tempering between  $\leq 500$  °C (LTT) and 5 by high-temperature tempering  $> 500$  °C (HTT). Fig. 4 shows examples of some of these microstructures.

Paper I investigates the  $T_0 - T_{28J}$  correlation of 39 different as-quenched S900, S960 and S1100 grade steels. Paper II utilises this data set and adds it to the pre-existing data set of Wallin [19], which includes a wider range of structural and nuclear pressure vessel steels and steel welds, effectively covering the steel grades from S275 to S1100. I take the 17 direct-quenched plus one reheated and quenched steel, originally produced for Kajjalainen et al. [9,131], to study the effects of microstructure on  $T_{28J}$  on a global scale in Paper III. Paper IV investigates the local properties affecting the  $T_{28J}$  and  $T_0$  with two laboratory hot-rolled martensitic steels. Paper V explores the low-temperature hydrogen embrittlement with S960QL heat-treated to as-quenched martensitic and martensitic-bainitic conditions, and I include a Q&T condition in this thesis. Table 2 presents the chemical composition range of these low-carbon low-alloy steels used in Paper I, and the compositions used in Papers III (A, B, C and S960), IV and V (S960QL).

**Table 2. The nominal chemical alloying composition range of the study materials (wt.%, Papers I, III, IV & V).**

	C	Si	Mn	Cr	Ni	Mo	Ti	Nb	B	P	S
Minimum	0.07	0.18	0.7	0.5	–	–	–	–	0	0.001	0.000
Maximum	0.15	0.30	1.8	1.2	4.1	0.50	0.03	0.04	0.003	0.011	0.005
A	0.07	0.2	1.4	1.0	–	0.02	0.02	0.04	0.001	0.009	0.001
B	0.08	0.2	1.8	1.0	–	0.01	0.02	0.04	0.002	0.011	0.000
C	0.09	0.2	1.1	1.1	–	0.15	0.02	0.04	0.001	0.009	0.001
S960	0.09	0.2	1.1	1.2	–	0.01	0.03	–	0.002	0.007	0.002
IV	0.13	0.2	1.1	0.7	–	0.16	0.03	–	0.002	0.007	0.002
S960QL	0.15	0.3	1.2	0.5	0.4	0.50	0.02	–	–	–	–

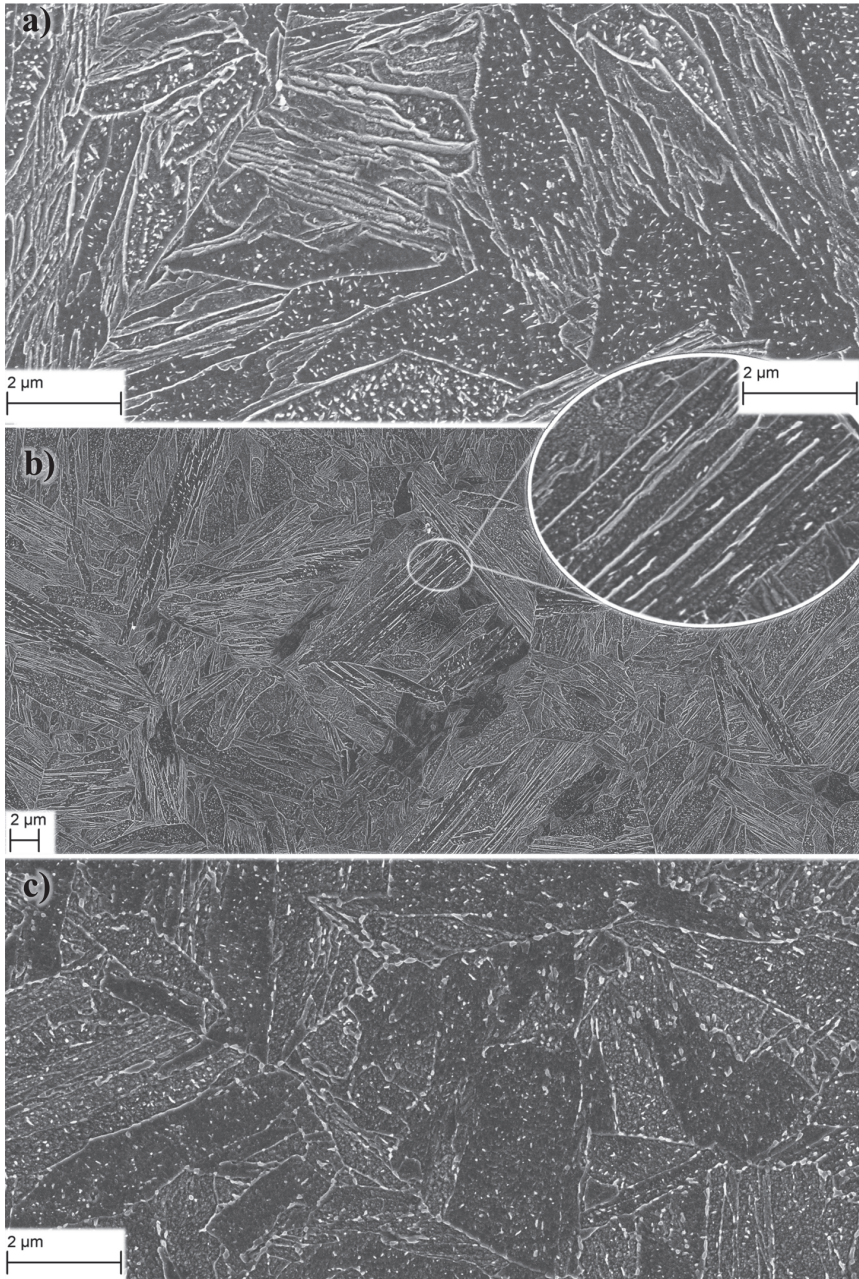


**Fig. 4. The many faces of cementite: a) As-quenched autotempered lath-martensite, b) mixed martensitic-bainitic microstructure, and c) quenched and tempered martensite.**

The full-scale direct-quenched steels of Paper III were produced by thermomechanically controlled rolling and direct quenching (TMCP-DQ) varying both the finish rolling temperatures (FRT) and  $R_{TOT}$ , the total rolling reduction of the prior austenite grains (PAG) below the non-recrystallisation temperature  $T_{NR}$ . FRT was varied between 950 and 800 °C, covering the temperature regions both above and below  $T_{NR}$ , and  $R_{TOT}$  between 23% and 79%. After the final passes, these steels were direct-quenched to room temperature at a rate of 50–70 °C/s. Together with the differences in the alloying contents, these ranges of processing parameters led to a wide range of microstructures and effective coarse grain sizes. The resulting martensite contents vary between 5% and 100% with the remaining consisting of different bainite morphologies (lower, upper, and/or granular bainite).

I used a 1 MN Carl Wezel laboratory rolling mill to produce hot-rolled reheated and quenched plates and a direct-quenched plate from the top and middle third of an experimental continuously cast slab and laboratory-cast ingots (Papers I, II and IV). Before the rolling, I reheated the blooms, sized to 62.5×80×270 mm, at 1050 °C for two hours to homogenise the microstructure. Annealing temperatures above 1100 °C caused abnormal grain growth and were hence avoided. Typical hot-rolling included four passes above  $T_{NR}$  and a total rolling reduction strain of 0.44 below it, resulting in a final thickness of 12 mm. Directly after the final pass at 850–920 °C, I quenched the plates in water with an average cooling rate of 90 °C/s, measured from the middle of the bloom with a thermocouple inserted into a hole drilled prior the rolling. Most of the plates went through an additional reaustenitisation at 850–900 °C and final water-quenching to room temperature to produce a fine, equiaxed prior austenite grain structure with a through-hardened martensitic microstructure.

The materials of Paper IV were taken from different thickness-wise sections of a width-wise central block from a continuously cast slab. This enables the separation of the central equiaxed cast structure that showed centreline segregation and was rich in inclusions (material “CL”) from the cleaner, more homogeneous columnar cast structure top section (material “MM”). These different sections were treated as described above.

For Paper V, I dehydrogenation annealed S960QL plates at 600 °C for four hours before heating to the austenitisation temperature of 900 °C for a 45-minute hold. After the austenitisation, quenching in water to room temperature produced autotempered lath-martensitic ATM. Interrupting quenching with a 10-second hold in air at 500 °C yielded the material denoted as AB with a martensitic – upper bainitic microstructure. Normal reheating, quenching, and tempering at 650 °C

produced the material denoted QL, which comprised tempered martensite. Passive cathodic protection hydrogen-charged the specimens to higher hydrogen contents than the initial dehydrogenized condition in an electrolyte resembling sea water for 94 hours before the tests. The potential of the system was approximately -1050 mV as measured against a standard Ag/Ag<sup>+</sup> reference electrode.

## 3.2 Methods

### 3.2.1 Mechanical testing

Impact toughness and fracture toughness tests were used to evaluate the materials focusing on the behaviour in the ductile-brittle transition temperature region, and to determine the impact toughness transition temperature  $T_{28J}$  and the fracture toughness reference temperature  $T_0$ . In addition, room-temperature tensile testing (EN 10002-1 [132] and EN ISO 6892-1 [133]) was used to measure the basic properties and to ensure the quality of the materials with 6–12.5 mm thick rectangular specimens cut with their tensile axes in the longitudinal (i.e. rolling) direction and the transverse direction. Eq. (10) of Ref. [14] estimates the yield strength at lower temperatures with temperature  $T$  expressed in Kelvins.

$$\sigma_{YS}(T)[\text{MPa}] = \sigma_{YS} + \frac{5.56 \times 10^4}{T} - 189 \quad (10)$$

Charpy-V notch (CVN) impact testing was used according to the standards EN 10045-1 [51] and EN ISO 148-1 [52] to determine the impact toughness transition temperature  $T_{28J}$  and upper shelf energy  $C_{V-US}$  of the 68 materials fitted with either Eq. (2) or (3). The most common temperature range used is +20 – -60 °C, but in some more brittle or ductile cases, the extended range spans from +40 °C down to -140 °C. Specimens were typically full-sized 55×10×10 mm, but also sub-sized specimens were used with thicknesses from 3 mm upwards. The sub-size values of 35 J/cm<sup>2</sup> transition temperature and  $C_{V-US}$  were converted to their full-size equivalents by the procedure of Ref. [19] and the equation in its conservative form given in Ref. [19], respectively. The estimated scatter of both  $T_{28J}$  and  $T_{50}$  is 10 °C in this thesis [19].

Fracture toughness testing and the determination of the fracture toughness reference temperature  $T_0$  were done on 55 materials according to the standard ASTM E1921 [10] using three-point bending test and mostly 10 mm thick SENB specimens with an a/W ratio of 0.5. Some specimens had 10% side grooves, and

some were thinner than 10 mm, the thinnest being 4 mm. Testing focused on the temperatures between -20 and -60 °C, but results were obtained from +5 to -100 °C. A constant displacement rate of 8.3E-3 mm/s has been used in the tests. This thesis presents the fracture toughness results as thickness-corrected to the estimated toughness of 1-inch thick specimens to determine the  $T_0$ , but also for the convenience of the reader and future comparability of the results.

Toughness testing was performed using both longitudinal-transverse (L-T) and transverse-longitudinal (T-L) specimens, Fig. 5. L-T specimens have their long side parallel to the longitudinal (rolling) direction, and the notch is in the transverse-normal (thickness) plane pointing in the transverse direction. T-L specimens have their long side parallel to the transverse direction and the notch is in the longitudinal-normal plane pointing in the longitudinal direction [134], Fig. 5. In five exceptions, only L-T data is available.

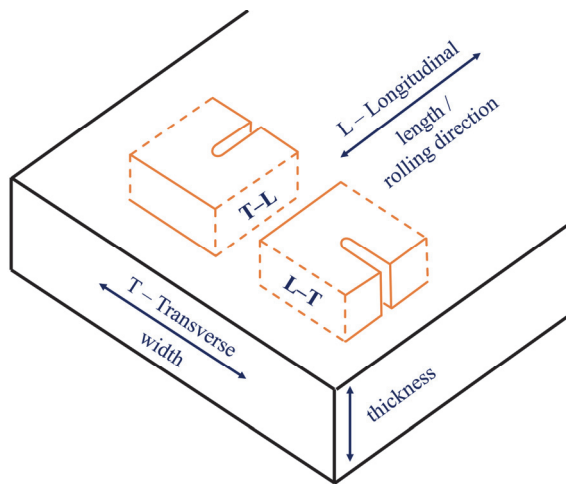


Fig. 5. Specimen and crack plane orientation for rectangular sections after Ref. [134].

### 3.2.2 Characterisation and statistical analyses

Several characterisation techniques are used in this research work to measure the chemical components, study the microstructures, and investigate the fracture surfaces. This thesis provides a brief explanation and advises the reader to turn to corresponding papers for further details. Paper I and II utilise previously available information about the compositions and microstructures of these steels concerned.

In Paper III, we characterise the prior austenite grain size, microstructure, and texture with a scanning electron microscope (SEM) and electron backscatter diffraction (EBSD) data acquisition and post-processing. Paper IV goes further and includes elemental analyses, inclusion mapping, and fractography. Fractography and kernel average misorientation (KAM) measurements of local deformation under the cleavage fracture initiation sites are the main characterisation techniques in Paper V.

Fractography starts with visual inspection of the fracture surfaces of SENB and CVN specimens. The areas containing the main initiation are sites identified with a light optical stereo microscope, and the river patterns that can be seen with higher magnifications with a SEM lead to the point of primary cleavage fracture initiation. Cutting metallographic sections in the thickness direction reveals the microstructure under these sites and enables the KAM measurement of the plastic deformation from selected specimen to reveal the effects of hydrogen.

We measured the bulk chemical compositions by optical emission spectrometry (OES) and with combustion analysis of the elements H, C, N, O and S. Large-scale through-thickness contents were determined from RD-TD sections extracted from different thicknesses using an OES with a 2 mm spot size (also for C and S). Electron probe microanalyser (EPMA) line measurements with a wavelength dispersive detector and a 10  $\mu\text{m}$  spot size provided us with local compositions over the thickness-wise central area.

Optical laser and stereo microscopes were the main tools to study the prior austenite grain structure and first observations of the fracture surfaces, respectively. We used SEM to study textures and fracture surfaces, as well as microstructures classified according to Ref. [135]. EBSD measurements from the mid-thickness provided the grain size and textural data and the energy-dispersive spectrometer (EDS) the composition of the inclusions found on the fracture surfaces. I determined all the grain size parameters as equivalent circle diameters (ECD) of the grains with high-angle boundaries ( $> 15^\circ$ ). The average effective grain size of the population is  $d_{\text{eff}}$  ( $> 0.3$  or  $0.4 \mu\text{m}$ ), and the sizes of the coarsest grains  $d_{80\%}$  and  $d_{90\%}$  correspond respectively to the effective grain size at 80% and 90% in the cumulative size distribution, and the volume-weighted average grain size  $d_v$  is calculated according to Lehto et al. [93].

In addition, I measured through-thickness macroscopic hardness, carbide size, and used XRD measurements of the microstructure and possible residual austenite. The hardness of martensite ( $HV_M$ ), calculated according to Blondeau et al. [136], Eq. (11), where  $V_R$  is the cooling rate, yields accurate estimates (Paper IV).

Inclusions were mapped by a third party from the cross-sections with an EDS and using a recognition threshold of 5 wt.% and if detected, iron was removed from the results. Inclusions classify into relevant categories according to their main component compounds and sizes. All the sizes of different measures are expressed as ECD values.

$$HV_M[\text{HV}] = 127 + 949C + 27Si + 11Mn + 8Ni + 16Cr + 21\log_{10}V_R \quad (11)$$

Basic statistical methods help to construct and validate the models proposed in this thesis, and to ensure the significance of the differences between the results. Bivariate analysis was used to tell whether the individual factors correlate with each other, and multiple linear regression analysis was used to build effective models. The two-sample t-test was used to measure the significance of the difference between two means. The Mann-Whitney 2-sample rank test [137] enables the comparison of the likeness of large data sets with non-normal distributions. The test is a non-parametric alternative to the 2-sample t-test of normal distributions which tells whether one distribution tend to be stochastically greater than the other. The null hypothesis indicates equality by default.

### **3.2.3 Modelling of hydrogen embrittlement**

We used the hydrogen-informed three-step procedure including cohesive zone modelling (CZM) [126,138] to simulate hydrogen embrittlement at -20 °C in an as-quenched martensitic microstructure. The procedure consists of:

1. Elastic-plastic finite element (FE) simulation. The specimen is loaded following the loading history of the experiments to get detailed information of the stress field.
2. Stress-driven hydrogen diffusion analysis. The hydrogen profile is obtained by taking into account the hydrostatic stress gradient given in the first step.
3. Elastic-plastic FE analysis with the added user-defined cohesive elements inserted over the mid-section. The cohesive strength is updated based on the uniform hydrogen degradation law (HDL) and according to the local hydrogen concentration information from the previous step.

To carry out these steps in ABAQUS, one needs to know a few basic things; the rate at which the hydrogen moves in the lattice, the behaviour of the cohesive elements, and their response to hydrogen. An average value of the effective diffusion coefficient  $D_{\text{eff}} = 2.3 \times 10^{-11} \text{ m}^2/\text{s}$  from Refs. [34,122,139–142] presents

the room temperature mobility of hydrogen for low- and medium-carbon as-quenched microstructures. I used an Arrhenius-type equation of Eq. (12), where  $R$  is the gas constant, fitted to the trend for martensitic steels reported in [143], to extrapolate this value to lower temperatures yielding  $D_{\text{eff}} = 5.9 \times 10^{-12} \text{ m}^2/\text{s}$  at  $-20 \text{ }^\circ\text{C}$  for the as-quenched martensite (material ATM).

$$D_{\text{eff}} \left[ \frac{\text{m}^2}{\text{s}} \right] = 8 \times 10^{-8} \exp \left( \frac{-20 \times 10^3}{RT} \right) \quad (12)$$

A modified Fick's law [144], Eq. (13), determines the local lattice hydrogen concentration ( $C_L$ ), where diffusivity is described with  $D_{\text{eff}}$ ,  $V_H$  is the partial molar volume of hydrogen in bcc ferrite,  $2.1 \times 10^{-6} \text{ m}^3/\text{mol}$ ,  $T_Z$  the absolute zero temperature, and  $\sigma_h$  the local hydrostatic stress component. The initial step assigns the measured hydrogen content as the initial hydrogen concentration  $C_L$  to every node in the model. Assuming that there is no significant hydrogen leak-out to the sub-zero alcohol surrounding the specimen during the test, the boundary conditions are insulated.

$$\frac{\partial C_L}{\partial t} = D_{\text{eff}} \nabla^2 C_L + \frac{D_{\text{eff}} V_H}{R(T-T_Z)} \nabla C_L \nabla \sigma_h + \frac{D_{\text{eff}} V_H}{R(T-T_Z)} C_L \nabla^2 \sigma_h \quad (13)$$

The polynomial traction-separation law (TSL) [145] describes the elastic behaviour of the cohesive elements. To overcome the common convergence problems at the point of instability in CZM, we incorporate a viscosity-like term [146] into the constitutive behaviour of the cohesive elements and express the viscosity regulated cohesive stress  $\sigma_v$  by Eq. (14), where the calibrated values are the critical cohesive stress  $\sigma_c = 5600 \text{ MPa}$  ( $2 \times$  the  $\frac{1}{2}\sigma_c$  given in Paper V), the critical cohesive separation  $\delta_c = 0.014 \text{ mm}$  and the viscosity parameter  $\zeta = 1 \times 10^{-3}$ . The strength of the cohesive elements as a function of lattice hydrogen is described by Eq. (15), a CZM-based uniform HDL calibrated by Yu et al. [129], where  $\sigma_{c,H=0}$  is the hydrogen-free critical cohesive stress.

$$\sigma_v(\delta) [\text{MPa}] = \frac{27}{4} \sigma_c \frac{\delta}{\delta_c} \left( 1 - \frac{\delta}{\delta_c} \right)^2 + \zeta \frac{d}{dt} \left( \frac{\delta}{\delta_c} \right), \delta < \delta_c \quad (14)$$

$$\frac{\sigma_c}{\sigma_{c,H=0}} = 0.421 e^{-2.227 \cdot C_L} + 0.579 \quad (15)$$

## 4 Results

### 4.1 $T_0 - T_{28J}$ correlation of as-quenched steels

Table 3 presents the broad range of characteristic mechanical properties acquired in the experiments. Only in one low-temperature tempered (LTT, L–T orientation) and two direct-quenched (T–L) steels is the fracture toughness reference temperature  $T_0$  above zero. The average transition temperatures are around the temperatures commonly used to specify minimum toughness levels for many steel grades. LTT are mostly on par with or inferior to the mean of the as-quenched materials (DQ & RQ). The high-temperature tempered (HTT) materials have consistently low transition temperatures and higher upper shelf toughness. For the as-quenched steels,  $T_0$  is persistently higher than the impact toughness transition temperature  $T_{28J}$ , on average 28 °C. Tempering at low temperatures, from 200 to 500 °C, widens the gap between the transition temperatures, and only high-temperature tempering > 500 °C can turn the difference to a conventional level ( $T_0 - T_{28J} \leq -3$  °C) obeying the  $T_{0-Est.1}$ .

**Table 3. Mechanical properties of the 55 steels expressed as mean [minimum, maximum] (DQ = direct-quenched, RQ = reheated and quenched, LTT = low-temperature tempered, HTT = high-temperature tempered).**

Material	$T_{28J}$ [°C]	$T_0$ [°C]	$T_0 - T_{28J}$ [°C]	$\sigma_{VS}$ [MPa]	$C_{V10-US}$ [J]
All	-60 [-175,0]	-35 [-132,21]	25 [-33,67]	1016 [670,1271]	154 [48,600] <sup>1</sup>
DQ	-67 [-175,0]	-37 [-132,21]	29 [9,67]	1043 [893,1250]	162 [48,600] <sup>1</sup>
RQ	-43 [-60,-25]	-20 [-44,-1]	23 [-13,39]	986 [950,1032]	135 [63,203]
LTT	-44 [-81,-22]	-9 [-39,21]	34 [15,63]	1068 [880,1271]	135 [79,170]
HTT	-81 [-106,-68]	-93 [-111,-63]	-12 [-33,8]	838 [670,999]	176 [102,250]

<sup>1</sup> Max. 300 J linearly proportional to area.

Neither the  $T_{0-Est.1}$ , Eq. (8) nor the  $T_{0-Est.2}$ , Eq. (9) are capable of describing the  $T_0$  values for these as-quenched materials. More importantly, both yield estimates that are on the non-conservative side. Only one exception falls within the confidence limits of  $T_{0-Est.1}$  (Fig. 6 a), a reheated and quenched steel possessing pronounced splitting behaviour and tested in T–L orientation, and less than half are within the limits of the  $T_{0-Est.2}$ . The addition of yield strength and upper shelf energy to  $T_{0-Est.2}$  brings the average slope closer to that of the as-quenched data set. However, it is apparent from Fig. 6 a) that there is a distinct linear trend between the measured transition temperatures  $T_0$  and  $T_{28J}$  for as-quenched low-carbon steels.

Since these correlations overestimate the level of  $T_0$  of low-carbon as-quenched ultra-high-strength steels, the data needs further regression analysis. The first suitable estimate has the form of Eq. (16) (Fig. 6 b), which fits the  $T_0/T_{28J}$  slope and the overall level between the transition temperatures. The resulting adjusted coefficient of determination  $R^2_{\text{adj.}}$  of 0.83 and the root-mean-square error (RMSE) of 11 °C are acceptable when compared to  $T_{0\text{-Est.1}}$  ( $R^2_{\text{adj.}} = 0.00$ , RMSE = 48 °C) and  $T_{0\text{-Est.2}}$  ( $R^2_{\text{adj.}} = 0.21$ , RMSE = 24 °C). Further additions of yield strength and/or upper shelf energy do not change the model in a significant manner for as-quenched materials, improving  $R^2_{\text{adj.}}$  by only 0.001 and RMSE by up to 0.2.  $T_{28J}$  is the only predictor that holds its individual significance in a t-test ( $p = 0.000$ , 95% confidence limits [0.7, 0.9]). Yield strength has a confidence interval [0.00, 0.08] and  $p = 0.083$  at best, and the confidence interval for upper shelf energy is [-0.05, 0.10] and  $p = 0.163$ . Thus, the addition of yield strength and/or upper shelf energy is questionable (at  $\alpha = 0.05$ ), as they produced more outliers and did not improve the estimates of  $T_0$  within this data set.

$$T_{0\text{-Est.3}}[\text{°C}] \approx 0.8 \times T_{28J} + 14, \sigma \pm 11\text{°C} \quad (16)$$

The non-parametric Mann-Whitney 2-sample rank test [137] validates the  $T_{0\text{-Est.3}}$  as a material property of as-quenched low-carbon steels. The null hypothesis of equal populations is rejected with  $T_{0\text{-Est.1}}$  and  $T_{0\text{-Est.2}}$  ( $p = 0.000$ ), but the  $T_{0\text{-Est.3}}$  has highly significant  $p = 0.660$  indicating that it produces equal estimates of the measured  $T_0$  values. Thus, the  $T_{0\text{-Est.3}}$ , Eq. (16) is valid material-specific fit for untempered martensitic and martensitic-bainitic low-carbon steels.

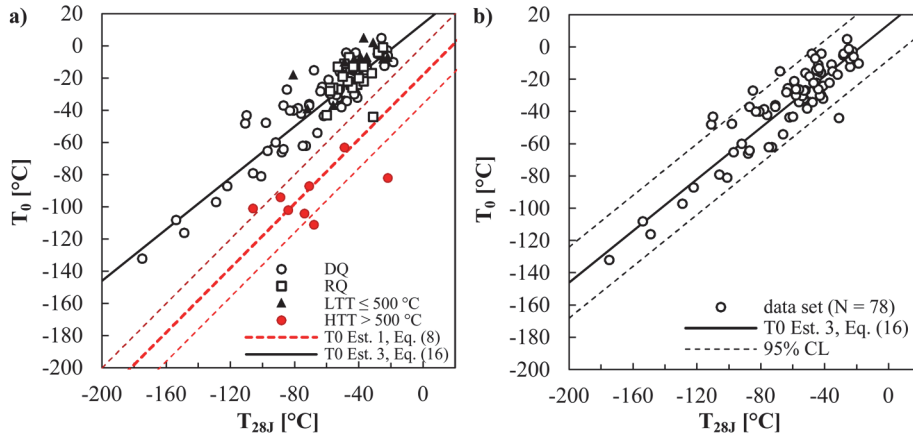


**Fig. 6. Applicability of Eq. [8] to the as-quenched (RQ, DQ), low-temperature tempered (LTT), and high-temperature tempered (HTT) UHSS microstructures, b) the  $T_0 - T_{28J}$  correlation of as-quenched steels. [Paper I, modified and reprinted by permission of Elsevier]**

Even though the additions of yield strength and/or upper shelf energy do not improve the  $T_0$  estimate within the data set of Paper I and this thesis, their effects need to be evaluated further. Fig. 7 shows their relationships with  $T_0 - T_{28J}$ . DQ, RQ and LTT follow the same trend of as-quenched microstructures in Fig. 7 a) which has an effect within the yield strength span of 391 MPa of a similar magnitude as in  $T_{0-Est.2}$ . The few ultra-high-strength HTT samples have more conservative  $T_0 - T_{28J}$ . Fig. 7 b) further demonstrates the differences between the HTT and the rest than any uniform trend between  $C_{V-US}$  and  $T_0 - T_{28J}$ . However, what is visible is that the lower the  $C_{V-US}$ , the higher the possible difference between the transition temperatures. This can also be due to fitting of the CVN data, where low applied  $C_{V-US}$ , either actual or due to insufficient information of the fraction of ductile fracture, can press the resulting  $T_{28J}$  lower than what it would be with the same data at the DBTT but high  $C_{V-US}$ . With respect to the four exceptionally high  $C_{V-US}$ , the use of Eq. (4) should be reassessed considering thin but very tough specimens.

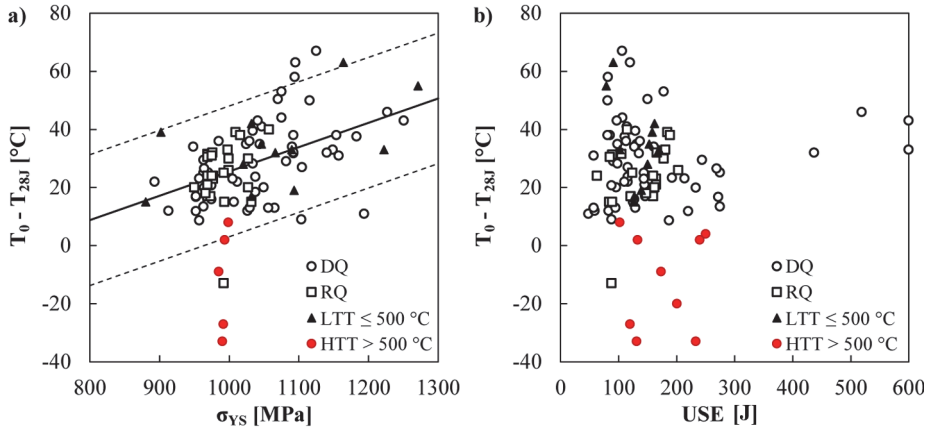


**Fig. 7. The elusive relationships between  $T_0 - T_{28J}$  and a) yield strength, b) upper shelf energy.**

Moving towards a general engineering application for a wider range of steels, Paper II combines 181 different sets of SENB tested data from Paper I, this thesis and Ref. [19]. Through a new three-dimensional regression analysis  $T_{0-Est.2}$  updates to a form of  $T_{0-Est.4}$ , Eq. (17). It is evident that the previous  $T_{0-Est.2}$  underestimates the effect of yield strength and overestimates the effect of upper shelf toughness on the correlation. That is, the coefficient of yield strength increases slightly, and the effect of upper shelf energy almost disappears, apart from the toughest of steels for which the term can have a stronger effect. Fig. 8 shows the applicability of the improved  $T_0 - T_{28J}$  correlation of  $T_{0-Est.4}$  for steels from S275 to S1300. It applies also to compact tension (CT, not shown here) specimen with an elevated constant of  $-79\text{ }^\circ\text{C}$  to account for the  $10\text{ }^\circ\text{C}$  bias between the SENB and CT specimen [10,19].

$$T_{0-Est.4} [^\circ\text{C}] \approx T_{28J} - 89 + \frac{\sigma_{YS}}{9} - \frac{c_{V-US}}{59}, \sigma \pm 18^\circ\text{C} \quad (17)$$

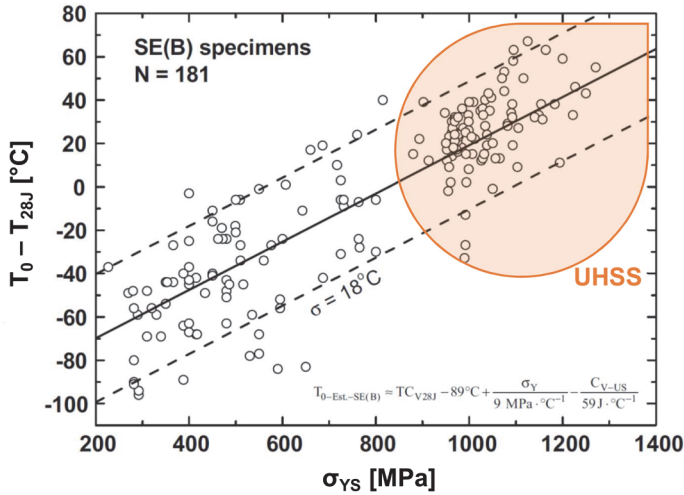


**Fig. 8. Improved  $T_0 - T_{28J}$  correlation of Eq. (17) applied over the whole yield strength range of structural steels. [Paper II, modified and reprinted by permission of Elsevier]**

## 4.2 Microstructural factors governing the transition temperature toughness

The impact toughness transition temperature  $T_{28J}$  ranges from  $-9$  to  $-126$  °C with the materials studied in Paper III. Martensite content has an apparent impairing effect on  $T_{28J}$  that improves almost linearly with decreasing martensite content. Increasing fraction of bainite phase constituents and decreasing grain size are associated with lower finish rolling temperatures and higher levels of austenite pancaking, respectively. Exceptions to this trend are the materials with low FRT, where the formation of more than 10% of granular bainite (GB) causes the grain size to abruptly increase, thus impairing both toughness and strength. The steel C (C880 and C840, the number indicates the given FRT) has both the best toughness and the best combination of toughness and strength, i.e. the highest absolute value of  $\sigma_{YS} \times T_{28J}$ . The coarse-grained reheated and quenched S960 and the S960 variants with FRT above  $T_{NR}$  have the worst toughness. The two test specimen orientations, L–T and T–L, follow each other closely ( $T_{28J} R^2 = 0.92$ ,  $T_{50} R^2 = 0.87$ ) with the values are on average 4 °C ( $T_{28J}$ ) and 6 °C ( $T_{50}$ ) higher for the T–L orientation. On average, there are no significant differences in yield strength between the longitudinal and transverse directions either, which allows us to combine the L–T and T–L data sets for further analyses.

From the different grain size measures, the reciprocal square root of the effective grain size corresponding to 80% in the cumulative probability distribution ( $d_{80\%}$ ) has the biggest influence on  $T_{28J}$ . However,  $d_{90\%}$  and volume-weighted average grain size  $d_v$  have explanatory power close to that of  $d_{80\%}$ . Yield strength and impact toughness transition temperatures show no direct, although the yield strength span of 326 MPa is rather limited in Paper III. Fig. 9 a) shows a bigger picture of  $T_{28J}$  versus  $\sigma_{YS}$  with the UHSS materials of this thesis ( $\sigma_{YS}$  range 422 MPa), mainly the increasing difficulty to achieve  $T_{28J}$  below about -120 °C in low-carbon as-quenched steels. In general, the parameters that correlate with the transition temperatures do not correlate with room temperature yield strength. Bivariate analysis shows that a stress intensity parameter  $\sigma_{d,ref}\sqrt{\pi d_{80\%}}$  (Fig. 9 b), coarse grain size (Fig. 10 a), and the area fraction of {100} cleavage planes close to the macroscopic crack plane (Fig. 10 b) are the best physical parameters to describe  $T_{28J}$ . I define the first parameter as the *dynamic reference toughness* ( $K_{Id,ref}$ ) given in Eq. (18), where room temperature yield strength is elevated with  $c_{\sigma_{YS}}$  to correspond to the dynamic yield strength ( $\sigma_{d,ref}$ ) at the strain rate of  $10^3 \text{ s}^{-1}$ , which is appropriate to a Charpy impact test, and crack length described with the *effective coarse grain size*,  $d_{ecgs}$ , which for now includes  $d_{80\%}$ ,  $d_{90\%}$  and  $d_v$  as potential descriptors. For  $\sigma_{YS} \geq 900$  MPa and A820 ( $\sigma_{YS} = 879$  in L and 849 in T orientation), we use a coefficient  $c_{\sigma_{YS}}$  of 1.2 according to the Ref. [147]. For milder strength steels, the  $c_{\sigma_{YS}}$  rises so that for S275 it is close to 2.

$$K_{Id,ref} [MPa\sqrt{m}] = \sigma_{d,ref}\sqrt{\pi a} = (c_{\sigma_{YS}} \times \sigma_{YS})\sqrt{\pi d_{ecgs}} \quad (18)$$

Based on the results of linear regression analysis, the dynamic reference toughness and the fraction of {100} cleavage planes within 15° of the macroscopic crack plane combine to form a model to describe the impact toughness transition temperatures ( $T_T$ ). This form of Eq. (19) is statistically most robust and can be used to estimate at least  $T_{27J}$ ,  $T_{28J}$  and  $T_{50}$ . The first term,  $K_{Id,ref}$ , is a failure initiation term linked to a propagation of a local Griffith crack, and the second term is associated with crack propagation and the size of the continuous cleavage fracture. Eq. (19) becomes Eq. (20) for  $T_{28J}$  ( $R^2 = 0.83$ , RMSE 14 °C) and Eq. (21) for  $T_{50}$  ( $R^2 = 0.79$ , RMSE 12 °C) using  $d_{80\%}$  as  $d_{ecgs}$  and with the outlier B920 excluded from the fitting. Fig. 11 presents the accurateness of fit of Eqs. (20) and (21).

$$T_T [°C] = c_1 \times K_{Id,ref} + c_2 \times \% \{100\} + c_3 \quad (19)$$

$$T_{28J} [°C] = 55 \times K_{Id,ref} + 3 \times \% \{100\} - 365, \sigma = \pm 14 \text{ °C} \quad (20)$$

$$T_{50}[\text{°C}] = 42 \times K_{Id,ref} + 2 \times \% \{100\} - 283, \sigma = \pm 12 \text{ °C} \quad (21)$$

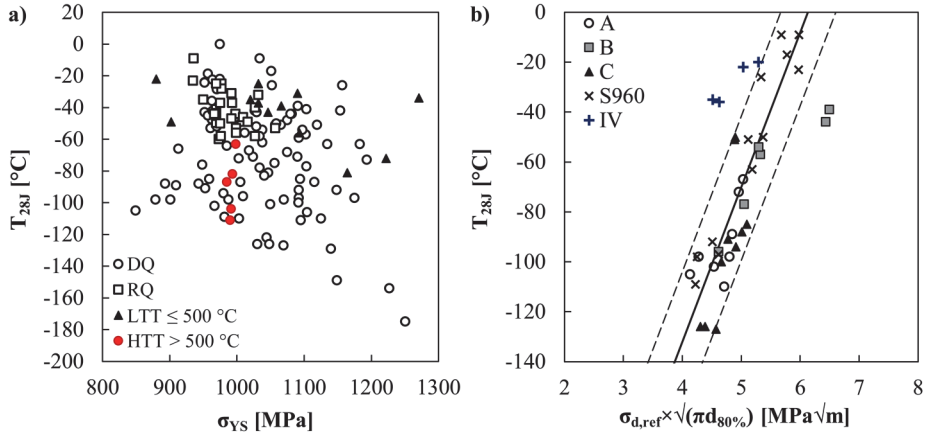


**Fig. 9. a) Lack of direct correlation between yield strength ( $\sigma_{YS}$ ) and impact toughness transition temperature  $T_{28J}$  with  $\sigma_{YS} = 849 \dots 1250$  MPa, and b) the effect of  $K_{Id,ref}$  calculated using the effective coarse grain size  $d_{80\%}$ . [Paper III, modified and reprinted by permission of Elsevier]**

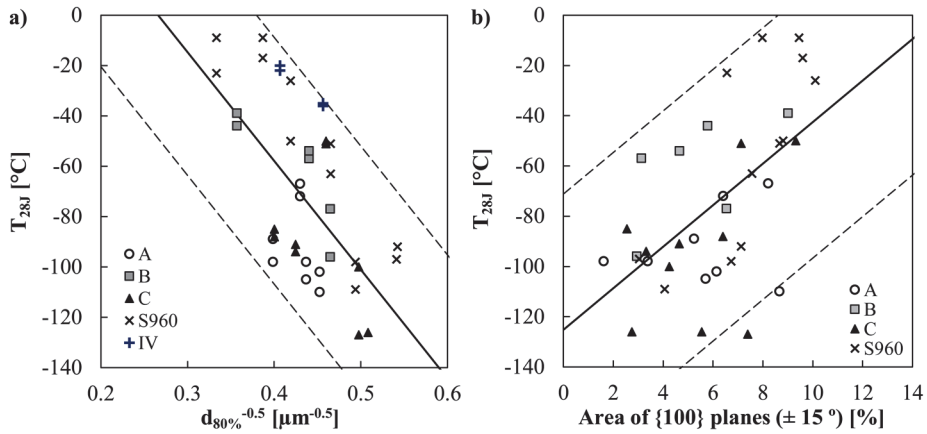


**Fig. 10. The effect of a) inverse square root of the effective coarse grain size and b) the area fraction of  $\{100\}$  planes in the notch plane on the impact toughness transition temperature  $T_{28J}$ . [Paper III, modified and reprinted by permission of Elsevier]**

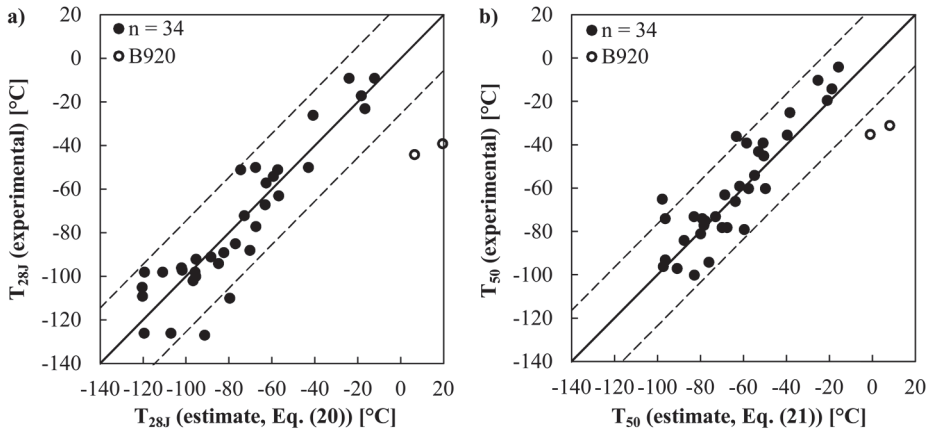


**Fig. 11. Estimated and experimental transition temperature values of a)  $T_{28J}$ , – Eq. (20), and b)  $T_{50}$  – Eq. (21). The open circles show the outlier B920 and the dashed lines the 95% confidence limits. [Paper III, modified and reprinted by permission of Elsevier]**

The results of Paper IV provide further insight into how the local microstructural features affect the toughness properties. The blooms, which are cut from the centreline (material CL) and off-centreline (material MM) positions from a single continuously cast slab, have no significant differences in  $T_{28J}$ , defined using the exponential fitting of Eq. (3), nor in the tensile properties. For both materials,  $T_{28J}$  is on a level of  $-50$  °C for the L-T orientation and around  $-35$  °C for the T-L orientation. The upper shelf toughness ( $C_{V-US}$ ) is better in the material MM in both orientations. The fracture toughness of the material CL is surprisingly good, having a significantly ( $p < 0.0001$ ) better  $T_0$  than the MM material, i.e.  $13$  °C lower for the L-T and  $16$  °C lower for the T-L orientation. CL has pronounced scatter of the individual data points in both impact and fracture toughness tests. Based on  $T_{28J}$ , the estimated  $T_0$  is far off on the non-conservative side with the conventional correlation of Eq. (8). Both the  $T_{0-Est.3}$ , Eq. (16) and the  $T_{0-Est.4}$ , Eq. (17) estimate the  $T_0$  results well. The initially surprising fact that the segregated and inclusion-rich CL material showed better fracture toughness  $T_0$  than the cleaner MM material can, however, be rationalised as shown below. We divide the material CL into a thickness-wise middle third ( $\pm 2$  mm from the centreline) and combined upper and lower thirds ( $> 2$  mm from the centreline), where appropriate. The material MM is presented as a whole due to its homogeneity.

The microstructure of both materials is through-hardened as-quenched martensite with varying degrees of auto-tempering. SEM examination showed that in CL, the level of non-auto-tempered lath martensite, i.e. showing no carbides or

very weakly visible carbides having the same colour and contrast as that of the matrix, is around 15%, which is 5% more than in MM. XRD measurements reveal no traces of residual austenite in either the MM or CL materials, which in practice means that the content is less than 1% and likely very finely distributed between the laths [38,42].

On the bulk level, the chemical compositions of the materials have only the slightest differences which, according to Eq. (11), should lead to a 6 HV higher hardness in the estimated hardness of CL. This difference is in line with the measured average through-thickness HV<sub>10</sub> hardness of 391 (± 2) and 395 (± 3) of MM and CL, respectively. The differences between the materials start to appear with the GD-OES measurements taken on planes normal to the thickness direction at various depths. The middle section of the CL shows clear segregation and enrichment of alloying elements at the centreline that reflect the measured hardnesses accurately: MM has almost uniform hardness throughout the thickness ranging from 375 to 402 HV<sub>10</sub>, whereas CL shows substantial scatter with a peak hardness of 448 HV<sub>10</sub> at the centreline and alloy-depleted tails with hardness as low as 367 HV<sub>10</sub>. EPMA measurements highlight the locally banded nature of the segregation. Mn, Cr and Mo concentrate on narrow bands in a size scale which matches with the stretches of very fine PAG (Fig. 12). The large inclusions are concentrated within these bands, (Fig. 12 b).

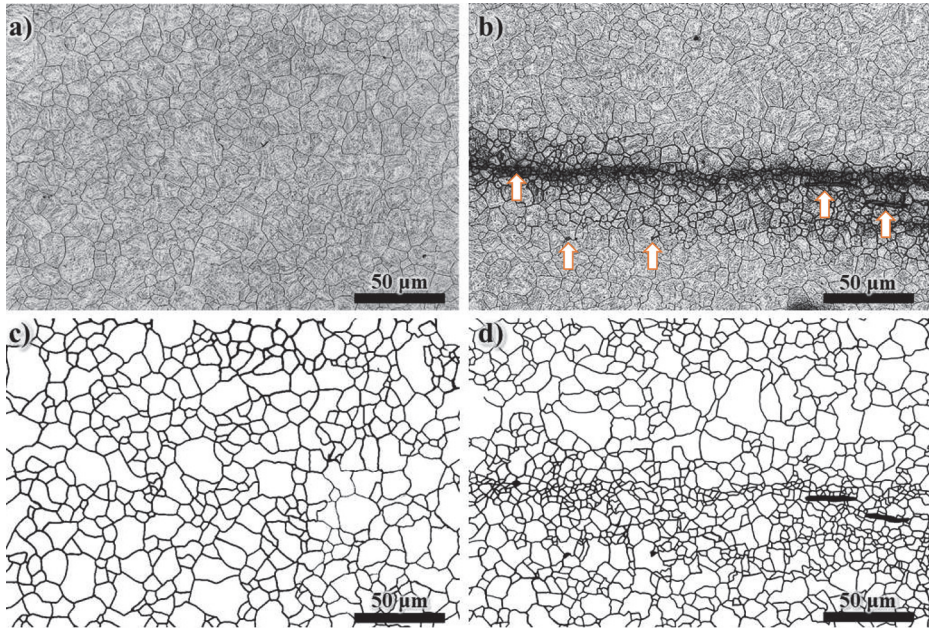


**Fig. 12. The prior austenite grain structure in the centreline of the materials MM and CL, the latter showing a typical segregation band. Laser scanning confocal microscope images of nital-etched specimens in a) and b), and binarised images showing the grain boundaries in c) and d). The arrows in b) point on inclusions. [Paper IV]**

The prior austenite grain structures separate the two materials further. MM has some distinct larger grains but otherwise quite uniform grain size distribution with an average PAG size of  $8.9 \mu\text{m}$ , Fig. 12 a) and c). In contrast, CL contains frequent segregation bands, Fig. 12 b) and d), which make the PAG distribution bimodal in the outer segments (avg.  $8.9 \mu\text{m}$ ), and press the average PAG size down to  $5.9 \mu\text{m}$  in the middle section, which is the most banded (Fig. 13 a). Cumulative probabilities highlight the differences in the coarse end of the effective grain size spectrum that is relevant considering toughness and strength (Fig. 13 b):  $d_{80\%}$  is  $6.05 \mu\text{m}$  in MM,  $4.80 \mu\text{m}$  in the outer sections of CL and  $3.43 \mu\text{m}$  in the middle third of CL, the last being 43% finer than in the competing MM.

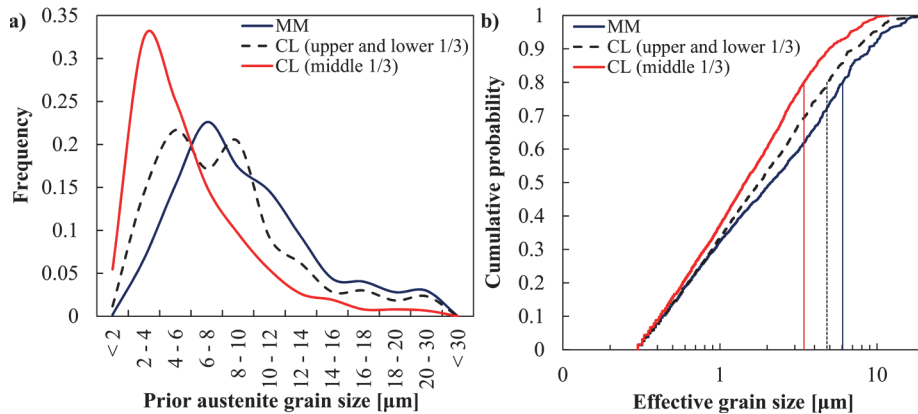


**Fig. 13. The differences in the grain sizes in the materials MM and CL: a) prior austenite grain size, b) cumulative probabilities of the effective grain size highlighting the effective coarse grain size  $d_{80\%-i}$ . [Paper IV]**

Mapped inclusions divide into four main groups based on the main element: aluminium, calcium, manganese, and titanium. Within these groups, there are nitrides, oxides, sulphides, and mixed type inclusions. CL contains larger inclusions, with an exception of CaOS, which are 23% bigger in MM. Furthermore, the largest inclusions in the CL material are concentrated in the middle third of the thickness, Fig. 14 a) and b). The size of the largest inclusions at 80% of the cumulative distribution ( $d_{80\%-i}$ ) is 3.3  $\mu\text{m}$  for MM and the outer segments of CL, and 5.3  $\mu\text{m}$  for the middle section of CL. Large CaOS and TiN inclusions or inclusion clusters are the most common failure initiator in the material MM, followed by grain boundary triple points. Abundant TiN and Ca-based inclusions could also be found near the local failure initiation sites in MM. TiN inclusions are the dominant reason of failure in CL, either as large individual inclusions, or accompanied by MnS, or as TiN clusters.

In the cases where inclusions were identified as initiation sites for the primary failure on the fracture surfaces of both SENB and CVN specimens, their sizes are bigger than the  $d_{80\%-i}$  values obtained from cross-sections through the bulk, i.e.  $4.6 \pm 0.8 \mu\text{m}$  and  $7.4 \pm 1.8 \mu\text{m}$  for the materials MM and CL, respectively. They correspond to the sizes at 94% and 90% in the cumulative size distributions. The average cleavage unit sizes found on fracture surfaces of the MM material are  $5.8 \pm 0.6 \mu\text{m}$ , which corresponds to the effective grain size at 79% in the cumulative grain size distribution. For the CL material, the average cleavage unit size is  $5.6 \pm$

0.4  $\mu\text{m}$ , which corresponds to 92% in the cumulative grain size distribution of the middle section.

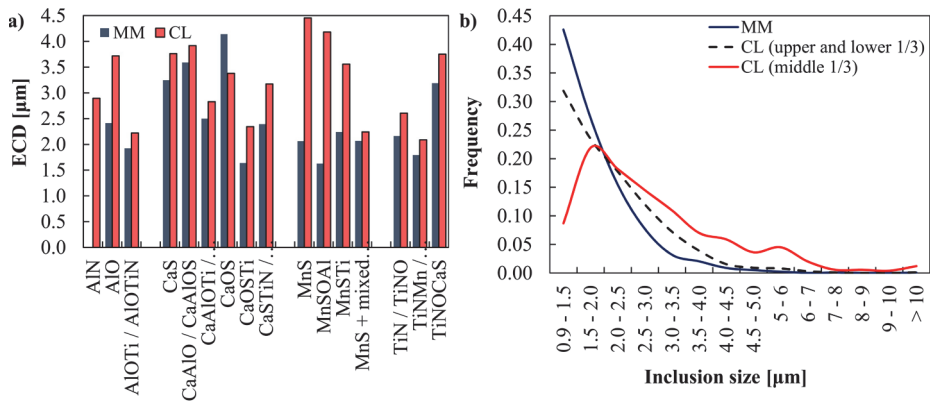


**Fig. 14. a) The sizes of the various inclusion types as equivalent circle diameters (ECD), b) comparison between the cleaner heterogeneous top-section MM and the inclusion-rich heterogeneous CL divided into the thickness-wise thirds. [Paper IV]**

The overall appearance of the fracture surfaces in both SENB and CVN specimens is typical for fractures in the DBTT range, consisting of brittle areas separated by frequent narrow ductile canvases. Macroscopically, the fracture surfaces are essentially flat in MM, whereas CL specimens frequently possess either one large or two to three smaller splits. The splits start with an inclusion and their walls contain very large, up to 30  $\mu\text{m}$  long, MnS inclusions as well as TiN inclusions. The fracture morphologies of the splits are diverse. The walls of the splits mainly have a combination of cleavage fracture and multi-void coalesced (MVC) ductile fracture, and there is a clear division between the sides of the V-shaped splits – the supposedly first formed side of the V-shaped split has a brittle appearance and the side that formed later shows a higher proportion of MVC. Shearing is present on most of the splits, but some smaller splits have a flat top and no sheared area. The splits are longer in the T–L than in the L–T oriented specimens, which reflects the length of the segregation bands on the given crack planes.

### 4.3 Hydrogen embrittlement at low temperatures

Table 4 shows measured total hydrogen contents and selected toughness test results for uncharged and hydrogen-charged materials. The hydrogen contents are unexpectedly high in the uncharged condition in as-quenched martensitic ATM, martensitic-bainitic AB, and quenched and tempered QL materials. The two H levels are anyway significantly different and thus comparable between the cases in all three materials. In both fracture toughness and impact toughness, AB is inferior to ATM. The fracture toughness of QL is higher than as-quenched microstructures, and its data points fall on the highly-scattered middle and upper part of the DBTT region yielding insignificant changes between the charging states and so only a provisional  $T_{0Q}$  for the hydrogen-charged state. Hydrogen-charging elevates both  $T_{28J}$  and  $T_0$  in the as-quenched ATM and AB, but the changes in  $T_{28J}$  are uncertain as the differences are statistically insignificant with respective p-values of 0.142 and 0.588. At the test temperatures studied,  $-20\text{ }^\circ\text{C}$  and  $-40\text{ }^\circ\text{C}$ , fracture toughness decreases 6% on average due to hydrogen charging and elevates  $T_0$  by  $8\text{ }^\circ\text{C}$  for ATM and  $6\text{ }^\circ\text{C}$  for AB. These changes in  $T_0$  are statistically significant in ATM and AB with respective p-values of 0.017 and 0.046.

**Table 4. Hydrogen content, transition temperatures  $T_0$  and  $T_{28J}$ , and fracture toughness at  $-20\text{ }^\circ\text{C}$  with their  $\pm$  standard deviations and (number of parallels).**

Steel	H [wt. ppm]	$T_{28J}$ [ $^\circ\text{C}$ ]	$T_0$ [ $^\circ\text{C}$ ]	$K_{Jc(1T)}$ , $-20\text{ }^\circ\text{C}$ [MPa $\sqrt{\text{m}}$ ] (number)
ATM, uncharged	$0.6 \pm 0.26$ (4)	$-58 \pm 10$ (15)	$-28 \pm 6.4$ (13)	$109.1 \pm 13.0$ (7)
ATM, H-charged	$1.1 \pm 0.17$ (3)	$-50 \pm 14.1$ (9)	$-20 \pm 7.5$ (8)	$104.3 \pm 5.6$ (5)
AB, uncharged	$0.9 \pm 0.25$ (4)	$-40 \pm 10$ (15)	$-19 \pm 6.3$ (14)	$100.5 \pm 4.9$ (6)
AB, H-charged	$1.4 \pm 0.24$ (3)	$-37 \pm 14.7$ (9)	$-13 \pm 7.2$ (9)	$93.3 \pm 5.4$ (6)
QL, uncharged	$0.9 \pm 0.35$ (4)	$-78 \pm 10$ (15)	$-87 \pm 7.2$ (9)	–
QL, H-charged	$2.0 \pm 0.28$ (3)	$-82 \pm 14.7$ (9)	$-89 \pm 11.1$ (3, $T_{0Q}$ )	$393.1 \pm 127.2$ (5)

Overall, the fracture surfaces of ATM are similar in both conditions with areas of essentially brittle cleavage, which are separated by frequent bands of ductile fracture. Both conditions produce small isolated intergranular fracture surfaces and patches of “flat” fracture, both associated with hydrogen embrittlement. These features are more frequent in the hydrogen-charged specimens with the higher H contents. Many of the cleavage surfaces in the H-charged specimens have fine lath-like features that correspond to quasi-cleavage. TiN particles populate the immediate vicinity of the local brittle fracture initiation sites in several cases.

KAM measurements of the sub-surface lattice distortion from the failure initiation sites reveal that the hydrogen-charged sample differs from the uncharged in that the level of distortion is clearly lower at levels under  $0.5^\circ$  and above  $1.5^\circ$  (Fig. 15 a). The fraction of the characteristic peak at  $1^\circ$  diminishes as the plastic deformation increases (unstressed reference  $\rightarrow$  H-charged specimens  $\rightarrow$  uncharged specimens).

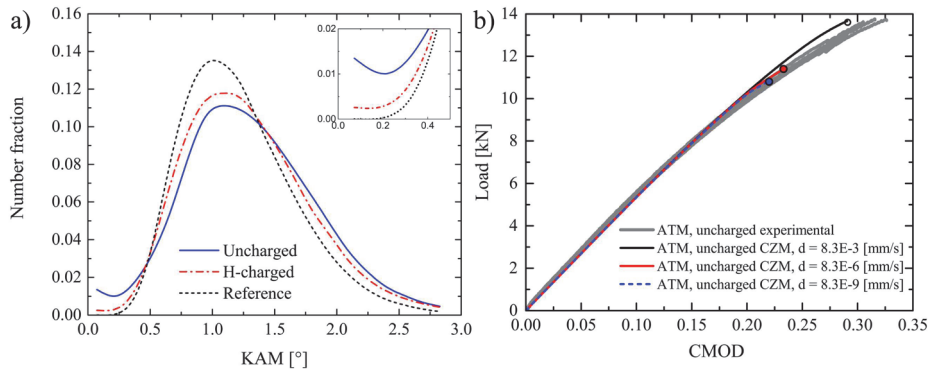


**Fig. 15. a) Decreasing lattice distortion with increased hydrogen content in ATM, b) CZM results for ATM with different displacement rates and H = 0.61 wt. ppm implying saturation with slower strain rates. [Paper V, modified and reprinted by permission of Elsevier]**

CZM modelling captures the experimental force-displacement behaviour in a reasonable manner by successful calibration of the cohesive parameters (Fig. 15 b). The curves of the 2D model hit the upper bound of the experiments. The failure point is at the complete separation of the tenth cohesive element corresponding to  $100 \mu\text{m}$  crack growth. This point coincides with the distance of the maximum opening stress with the average distance of the failure initiation site from the pre-fatigued crack tip in the experiments ( $150 \mu\text{m}$ ). The model predicts profound degradation of toughness for the hydrogen-charged case with  $\text{CMOD} -25\%$ ,  $F_{\text{max}} -17\%$  and  $K_{\text{JC}(1T)} -20\%$  compared to the experimental results at  $-20^\circ\text{C}$  (Paper V). Different simulated displacement rates from  $8.3 \times 10^{-3}$  to  $8.3 \times 10^{-9}$  mm/s predict the toughness to decrease further with the slower strain rate of  $8.3 \times 10^{-6}$ , but is almost the same with  $8.3 \times 10^{-9}$  (Fig. 15 b) with both H contents.

## 5 Discussion

### 5.1 On the $T_0 - T_{28J}$ correlation

As a material property, the best-fit  $T_{0-Est.3}$  of Eq. (16) provides accurate estimates for as-quenched steels of various bcc phase constituents and from different origins and process routes, Fig. 6 a) and b). The unifying properties are that they all have a hardened microstructure, low carbon content and yield strength of about 900 MPa or more. Based on that, it should apply equally to hardened welds, too, as already shown in Refs. [148,149]. Given the simple form of  $T_{0-Est.3}$ , it serves as a good first estimate of  $T_0$  and especially for welds, as it is more elaborate to extract other mechanical parameters from them.  $T_{0-Est.3}$  applies also to the low-temperature tempered materials (LTT).

The open questions that remains are: can one allow the slope of  $T_{28J}$  to differ from unity and how to address the remaining 20%. If one must have  $T_0/T_{28J} = 1$ , the correlation of  $T_{0-Est.3}$  gets the form of  $T_{0-Est.5} \approx T_{28J} + 28 \text{ }^\circ\text{C}$ ,  $\sigma \pm 14 \text{ }^\circ\text{C}$ , based on the DQ, RQ and LTT materials with  $n = 94$  (50 materials, DQ and RQ tested in L-T and TL orientations, LTT in L-T only) and  $\sigma_{YS} = 880 \dots 1271 \text{ MPa}$ . The fit is ok, but it does not change the difference in the slope. Whether this difference is just due to sampling or the physical discrepancies between the FT and CVN testing deserves further research.

Zhang and Knott [150] expect the minimum stress intensity factor  $K_{MIN}$  to be 65  $\text{MPa}\sqrt{\text{m}}$  and 81  $\text{MPa}\sqrt{\text{m}}$  for two homogeneous as-quenched martensitic steels, significantly higher than the standard value of 20  $\text{MPa}\sqrt{\text{m}}$ . For bainitic and mixed martensitic-bainitic microstructure, the  $K_{MIN}$  is close to 20  $\text{MPa}\sqrt{\text{m}}$  [150]. The FT test data gathered in this thesis support a possible higher  $K_{MIN}$  with the extrapolated lower-bound fracture toughness at the 0.01% probability level reaching up to 40  $\text{MPa}\sqrt{\text{m}}$ , but the linear fit is definitely not quite as good as in Ref. [150], and the lowest used test temperature of  $-100 \text{ }^\circ\text{C}$  is too high to exclude an additional drop in  $K_{Jc}$  level at lower temperatures. Furthermore, the determination of  $K_{MIN}$  can be quite ambiguous as discussed by Wallin [19]. If as-quenched martensite has a distinct high (apparent)  $K_{MIN}$ , it could be due to the compressive residual stresses (Type I - homogeneous long-range stresses) in the thickness-wise central area of the plates. At the lower shelf and in the linear elastic analyses, the residual stress component is additive to the total stress intensity [49], but the magnitude of the residual stresses after the pre-fatiguing demand proper quantification [151]

although compressive residual stresses can be unaffected by the advancing crack front [152]. This thesis will stay uncertain about how much these contribute to the  $T_0 - T_{28J}$  correlation.

High-temperature tempered (HTT) steels obey the conventional correlation ( $T_{0-Est.1}$ ), but the LTT, RQ or DQ do not (Table 3). The somewhat larger carbides of the Q&T [29,30] steels and of LTT steels tempered at 500 °C [153], combined with the fractographic evidence of the larger inclusions nucleating the brittle fracture (Paper IV), nullify the hypothesis that the carbides could alter the  $T_0 - T_{28J}$  correlation between these steels. With a lack of direct evidence relating carbides to the primary cleavage crack origin [71], in the presence of readily available larger cleavage fracture initiators, and with the  $\sigma_f \approx 11\,000$  MPa (Eq. (1):  $\gamma_{eff} = 7\text{ J/m}^2$  [66],  $d = 0.04\ \mu\text{m}$ ) for a coarse carbide, they seem quite unrealistic origins of failure even for the cases with unfound primary cleavage fracture initiators because readily available larger brittle inclusions fail at much lower stress levels. The differences left are the dislocation density, hydrogen content and sensitivity to it, and residual stresses.

Lower initial dislocation density [154] provides Q&T steels with better deformation capability, but they have also lower strain-hardening compared to as-quenched steels [155,156]. A material with low strain-hardening will have a larger plastic zone ahead of the fatigue crack or notch, which leads to a larger volume experiencing high triaxial stresses. In a larger volume, there is a higher probability of encountering a microstructural feature capable of producing a critically sized microcrack. On the other hand, a material with high strain-hardening will accumulate higher stresses ahead of the crack tip [54] and will so be more likely to fail at a given stress intensity. This could largely explain the lower toughness of the as-quenched steels.

In order to evaluate the effect of hydrogen between the as-quenched and quenched & tempered steels to be comparable, one would need to have the two microstructures with approximately the same toughness level and tested at the same temperature. Unfortunately, the quenched and tempered QL steel in Paper V was clearly tougher and on the other end of the ductile-brittle transition region (Table 4), so comparison is not possible between the materials nor within the QL between the two hydrogen contents. The measured total hydrogen content of 0.6 wt.ppm and the tensile strength of the material ATM coincide with the 20% loss of ductility based on the correlation of Refs. [124,125] (Paper V). Assuming that this translates to a similar loss of toughness around the  $100\text{ MPa}\sqrt{\text{m}}$  level when compared to zero-hydrogen case, the hydrogen-free ATM would have 16 °C lower  $T_0$  ( $K_{Jc} / 0.8$ ). If

the impact toughness would also be similarly affected (which is not the case), the hydrogen-free  $T_{28J}$  would be only 5 °C lower. This implies that the shift in the transition temperature values due to hydrogen could partially explain the higher  $T_0 - T_{28J}$  difference of as-quenched martensitic steels and contribute to the 20% missing from the unity of Eq. (16).

The effect of residual stresses on the  $T_0$  and  $T_{28J}$  would likely demand a thesis of its own. Even if they constitute to a strengthening property for as-quenched martensite [33], the inhomogeneous short-range microstresses (Type II) and their local direction and magnitude make their transferability to the scale of a test specimen challenging [157]. Hutchinson et al. [33] demonstrated that the microstresses may well explain the relatively low yield strength compared to the tensile strength of as-quenched martensite. Low-temperature tempering raises  $\sigma_{YS}$  by relieving some of these stresses (up to 50% at 250 °C [32]) while  $\sigma_{TS}$  stays almost unchanged. Table 3 shows the same elevation of  $\sigma_{YS}$  with LTT. Note with low  $\sigma_{YS}$  in Table 3 that here  $LTT \leq 500$  °C: materials tempered  $\leq 250$  °C have elevated  $\sigma_{YS}$  and the materials tempered at 500 °C have lowered  $\sigma_{YS}$  when compared to their as-quenched counterparts. A higher “true”  $\sigma_{YS}$  might explain the effect of  $\sigma_{YS}$  on the  $T_0 - T_{28J}$  difference (Fig. 7 a), the difference between as-quenched and Q&T steels, and the underestimation of the effect of  $\sigma_{YS}$  on the  $T_{0-Est.2}$  [19], Eq. (9).

Reassessment of the effects of  $\sigma_{YS}$  and upper shelf toughness  $C_{V-US}$  (Fig. 7 b) leads to  $T_{0-Est.4}$  of Eq. (17). UHSSs cover now around half of the whole data set of 181 samples. The adjustment to the coefficient of  $\sigma_{YS}$  and suppression of the effect of  $C_{V-US}$  enable the estimation of  $T_0$  based on the data with  $\sigma_{YS}$  between 248 and 1271 MPa. Even though the effect of  $C_{V-US}$  is small for most cases, it is included to increase the accuracy of the estimate for both the toughest and most brittle cases, acting as a minor corrective factor for tearing resistance. If  $C_{V-US}$  is omitted from the estimate, its effect (average  $-2$  °C  $\pm$  2 °C) can be included in the constant term by lowering it by 2 °C [158] or as a more conservative approach the constant term can be left unchanged. The outliers in the data set tend to be on the conservative side of the 95% scatter bands. With this model, the majority of the DQ, RQ and Q&T materials fall into the same band within the confidence limits of Eq. (17) that are broader than with  $T_{0-Est.3}$  and  $T_{0-Est.5}$  ( $\sigma = 18$  °C vs. 11 °C and 14 °C, respectively). Thus, it appears that  $T_{0-Est.4}$  can be used as a general  $T_0 - T_{28J}$  correlation regardless of steel strength or quality.

Considering the temperature dependency of MC, Eq. (6), with the ultra-high-strength steels from Ref. [159], the analysis shows a slight decrease for the  $\sigma_{YS}$

dependent  $c$  of Ref. [19] from the standard  $0.019\text{ }^{\circ}\text{C}^{-1}$  to  $0.017\text{ }^{\circ}\text{C}^{-1}$ . The differences are within  $3\text{ }^{\circ}\text{C}$ , so also the standard MC seems to be fairly applicable for UHSS.

## 5.2 On the microstructural features

The size of the coarsest discontinuities in the microstructures that can nucleate a microcrack seems to be the property that defines the toughness in the ductile-brittle transition region. Such readily available features are coarse grains and inclusions (Fig. 14).

As regards the coarse grains, their size can be described using the effective coarse grain size  $d_{\text{ecgs}}$ , expressed as an equivalent circle diameter, at either the 80% ( $d_{80\%}$ ) or 90% ( $d_{90\%}$ ) points in the cumulative effective grain size distributions. Combined with dynamic yield strength,  $d_{\text{ecgs}}$  allows the linking of impact toughness transition temperatures to the established dynamic reference stress intensity  $K_{\text{Id,ref}}$ .  $K_{\text{Id,ref}}$  relates to the propagation of a local Griffith crack. For small changes, a given percentage drop in  $\sigma_{\text{YS}}$  lowers  $K_{\text{Id,ref}}$  approximately twice as much as an equal percentage drop in  $d_{\text{ecgs}}$ . Considering that a given steel class must have a certain minimum yield strength, the refinement of  $d_{\text{ecgs}}$  is the only viable mean to achieve lower toughness transition temperatures. The semi-physical model of Eq. (19) uses the amount of  $\{100\}$  cleavage planes as a propagation term to estimate the transition temperatures, here in as-quenched steels with fully and partly martensitic microstructures.

Fractographic evidence shows that both large grains and large inclusions, i.e. the inclusions at 80–90% of the cumulative inclusion size distribution, facilitate the primary cleavage fracture initiation. In this regard, the inclusions should be incorporated to Eq. (19).

Both the lowest  $T_{28J}$  and the best absolute combination of toughness and strength come with mixed phase constituents of 70% ATM + 30% UB (C880) and 25% ATM + 70% UB + 5% GB (C840). The apparent inferiority of fully or almost fully martensitic materials is directly related to the coarse grain size of the materials in Paper III due to the limitations of the chosen process route of TMCP-DQ. The same applies to the materials with over 10% of granular bainite (GB) because its excessive formation enlarges  $d_{\text{ecgs}}$ .

Considering toughness properties, the effective coarse grain size is best described with  $d_{80\%}$  and  $d_{90\%}$ , which are also supported by the fractographic findings. Of  $d_{80\%}$ ,  $d_{90\%}$  and  $d_v$ ,  $d_{80\%}$  has the best correlation with  $T_{28J}$  through the  $K_{\text{Id,ref}}$  term (Fig. 9 b). Using  $d_{90\%}$  in the formula for  $K_{\text{Id,ref}}$  produces larger scatter

than using  $d_{80\%}$ , which is likely due to higher sample-dependent variance in the top range of the grain size populations. On the other hand, based on the fractographic evidence  $d_v$  is too small to cause a failure among present coarser grains.

The importance of the coarsest grains can be understood by the double-barrier model as presented by Lambert-Perlade et al. [77]. In the propagation-controlled DBTT region, the critical event for the local brittle fracture is the propagation of a microcrack through the high-angle grain boundaries. Large grains and large inclusions can be such weakest links to form the microcracks. In the identified cases, inclusions caused more failures than grain boundary triple points. Large TiN inclusions or clusters of inclusions are the most common failure initiators in both the homogeneous clean MM and heterogeneous inclusion-rich and segregated CL. Interestingly, in order to initiate the failure of the specimen, a large brittle unit needs to be located in a coarse-grained matrix to propagate the microcrack far enough to accumulate a critical level of damage. In this criterion, the first barrier is most likely the interface of the brittle inclusion and the coarse grain in which it is located, and the second barrier the boundary surrounding the coarse grain. The observations of large inclusions in a fine-grained ductile matrix inside the fracture process zone support this finding.

Assuming the Griffith crack criterion of Eq. (1),  $\gamma_{\text{eff}} = 100 \text{ J/m}^2$  [160] and setting the failure criterion to  $\sigma_f \approx 3 \times \sigma_{\text{YS}}$ , which is appropriate for small-scale yielding in a non-hardening material, the stress levels for the fracture toughness specimens in Paper IV are in line with the experimental findings (Fig. 16). In the homogeneous MM  $d_{\text{ecgs}}$  ( $d_{80\%}$  and  $d_{90\%}$ ) yield  $\sigma_f$  around the criterion level, and the failure initiating inclusions are slightly above it. When a suitably large inclusion is sampled within the process zone, it is easy for the crack to propagate through the coarse-grained matrix (MM, outer 1/3s of CL). In the middle third of the inclusion rich CL, an average large inclusion to-be cracked meets the criterion with ease, especially inside the segregation bands, but the propagation of the crack over the coarse grains is more difficult due to the smaller grain size, Fig. 12 and Fig. 13 b).

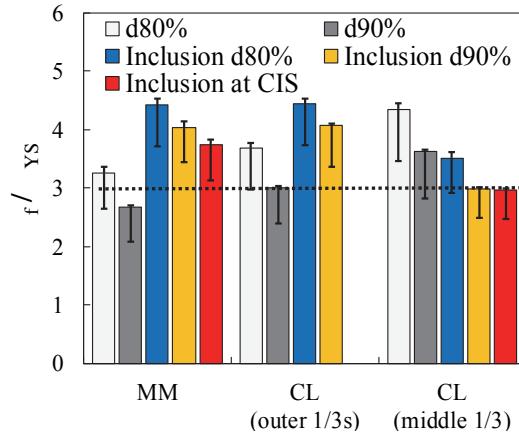


**Fig. 16. The relative critical failure stress according to a modified Griffith criterion in the materials MM and CL. The bars are scaled to approximated quasi-static yield stress at -40 °C, upper limits to -20 °C ( $T_0$  region), and lower limits to dynamic yield strength at -40 °C ( $T_{28J}$  region). [Paper IV]**

The analysis above justifies the application of  $d_{ccgs}$  to both the grains and inclusions when the failure initiators are known. After the local cleavage crack initiation, the crack propagation follows. The measures of the  $\{100\}$  planes parallel to the crack propagation determine how far a cleavage crack can propagate before encountering the first possibilities for crack arrests. Thus, the area fraction of  $\{100\}$  planes parallel to the crack plane ( $\pm 15^\circ$ ) is a simple and easily available measure for unhindered crack propagation. The lower the  $\{100\}$  fraction, the more probable local crack arrests are during the fracture process. Fig. 17 shows an example how the lower finish rolling temperature and higher austenite pancaking decrease the grain size and chop the  $\{100\}$  to fine and discontinuous islands, although clear textural banding is also visible. From the high-FRT C920 (Fig. 17 a and b) down to low-FRT C840 (Fig. 17 c and d)  $T_{28J}$  decreases by 76 °C while  $\sigma_{YS}$  decreases only by 19 MPa due to the presence of softer phase constituents (ATM 90%  $\rightarrow$  25%).

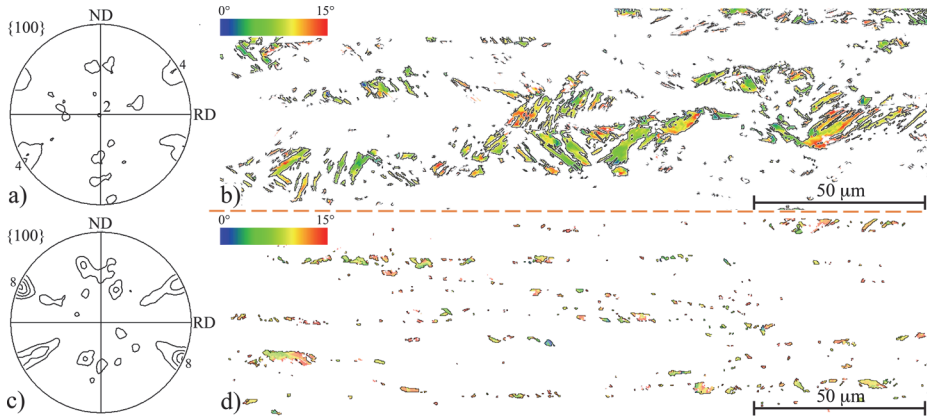


**Fig. 17. {100} pole figures and distribution of grains having {100} planes within 15° of the notch plane for material C. a) and b) high FRT and low  $R_{TOT}$  (C920), c) and d) low FRT and high  $R_{TOT}$  (C840).  $T_{28J}$  improves 76 °C in due to refined coarse grain size and smaller discontinuous {100} planes. [Paper III, modified and reprinted by permission of Elsevier]**

$K_{Id,ref}$  links the yield strength to  $T_{28J}$ . With just the dynamic reference toughness and the area fraction of {100} planes, Eq. (19) is the most robust model to describe the impact toughness transition temperatures (here  $T_T = T_{27J}$ ,  $T_{28J}$  and  $T_{50}$ ), Fig. 11. Note that Eq. (19) to Eq. (21) apply irrespective of the test specimen orientation with respect to the rolling direction due to the inclusion of the fraction of {100} planes within 15° of the main fracture plane and with assumed essentially equal  $d_{ecgs}$  between the longitudinal and transverse planes. Proper EBSD measurements yield the necessary data for the use of the model, and because of the semi-physical nature of the Eq. (19) it should also apply to other microstructures than the studied as-quenched ones.

As the results of Paper IV show, segregation is not necessarily bad, although large brittle inclusions should always be avoided if possible. As demonstrated, it can produce a laminar structure, where the largest inclusions are surrounded by the smallest grains (Fig. 12). The banded/laminar structure promotes splitting [97,103–105], which increases the toughness in the DBTT regions [97,105–107], naturally in CVN test, but also in FT tests when the splits formed before the global failure do not surpass the pop-in criterion in ASTM E1921 [10]. This is the case with 7 specimens in material CL, of which 6 had the highest toughness at the given test temperatures. This refinement of the prior austenite grain size is essential to good low-temperature toughness properties, as it limits the maximum size of the coarsest effective grains can possess as explained in Section 2. The best TMCP-DQ

production practices to achieve this are the utilisation of low FRT and maximum  $R_{TOT}$ , as long as the formation of granular bainite is suppressed.

### 5.3 On the hydrogen embrittlement

Lower fracture toughness at  $-20\text{ }^{\circ}\text{C}$  and  $-40\text{ }^{\circ}\text{C}$  (Table 4), less plastic deformation under the fracture surface as measured with kernel average misorientation method (Fig. 15 a), HE-related fractographic evidence of mixed “flat” features and quasi-cleavage, and cohesive zone modelling results (Fig. 15 b) point to the same conclusion: higher hydrogen content is able to induce a reduction in toughness and deformation capabilities in sub-zero temperatures, in the quasi-static fracture test at a displacement rate of  $8.3 \times 10^{-3}\text{ mm/s}$ . The increase in  $T_0$  is small but significant in the martensitic ATM and martensitic-bainitic AB. However, the changes in  $T_{28J}$  are insignificant. This indicates that hydrogen affects the  $T_0 - T_{28J}$  correlation.

As measured with the KAM method, the lower lattice distortion with higher hydrogen content is in agreement with the hydrogen enhanced decohesion mechanism [110,119]. The inherent  $1^{\circ}$  is due to the shear strains from martensitic transformation [39,43] in addition to the contribution of the lath-boundaries [43]. Deformation lowers the fraction of that characteristic peak, shifts it slightly towards higher misorientation, and elevates both the lower and upper tail (Fig. 15 a). The agreement is good with a clear order from the unstressed reference level to slightly deformed hydrogen charged cases and finally to the uncharged case with 0.5 wt.ppm lower bulk H content (Table 4).

The three-step HE simulation produces satisfactory results compared to the experimental data with well captured behaviour of both the global and local failure. I emphasise again that in the simulation, as supported by the KAM observations, hydrogen reduces the cohesive strength of user-defined elements on the predefined crack path. The model predicts a pronounced decrease in toughness in the hydrogen-charged case (Fig. 15 b). Slight conservativeness can be regarded as beneficial considering industrial applications.

The over-conservative predictions might be caused by the omission of trapped hydrogen in the current model and possibly by the material differences used in the original calibration of the HDL [129]. Although this can cause the difference, the effect of pre-existing traps in martensitic steels is already incorporated with the definition of the effective hydrogen diffusion coefficient acquired from the literature and adjusted to the test conditions. In this study, the measured total hydrogen content of ATM is considered as readily diffusible lattice hydrogen,

justified with the limited plasticity of UHSS [161] and previous successful modelling with excluded trapped hydrogen [162].

Pallaspuro et al. [163] iterated from this assumption on the basis of the HDL of Eq. (15) that the lattice hydrogen content of ATM is about one half of the total hydrogen content in the hydrogen-charged condition. The proportion of diffusible hydrogen  $C_L$  is a decreasing function of the total hydrogen content (best-fit  $C_L = -0.04 \times H^2 + 0.63 \times H + 0.06$ , based on the data of Ref. [164]). The proportion of 47.5% ( $C_L \approx 0.5$  wt.ppm) brought the CZM results in line with the experimental observations of this thesis.

The displacement rate of the experiments,  $8.3 \times 10^{-3}$  mm/s, is not slow enough at  $-20$  °C for H to achieve equilibrium with the hydrostatic stress state. For this reason, the simulated toughness drops further down with the rate of  $8.3 \times 10^{-6}$  mm/s, but not anymore with  $8.3 \times 10^{-9}$  mm/s. This implies that a displacement rate of  $8.3 \times 10^{-6}$  mm/s is small enough for hydrogen to achieve equilibrium concentration at  $-20$  °C and therefore the deleterious effect of H saturates, as shown in Ref. [129]. Still, even with the relatively short time for hydrogen to diffuse to the crack front, the time corresponding to the experimental case, the difference in the H content between the uncharged and H-charged condition is enough to decrease the simulated toughness. These experimental and simulational findings are consistent with HEDE theory, and with the fractographic findings, with the hydrogen-enhanced-plasticity mediated decohesion theory of Ref. [24].

Here, the effects of differing displacement rates, i.e. eventual diffusion times, were studied only numerically. However, Depover et al. [165] got similar results experimentally by varying the displacement rates and initial hydrogen contents, and found that extent of HE increased with lowering the test speed and that the hydrogen-related features were present on the fracture surface over a distance H could diffuse in given test conditions. In the experimental case of Paper V (displacement rate of  $8.3 \times 10^{-3}$  mm/s), the diffusion distance is in the order of 25  $\mu\text{m}$  ( $x = (t \times 2D_{\text{eff}})^{1/2}$ ) and slightly more based on the distance between the hot-spots in Fig. 13 of Paper V, so only H-affected region is measured with KAM. For the simulated displacement rate of  $8.3 \times 10^{-6}$  mm/s and slightly shorter total displacement to failure, the diffusion distance would be in the order of 850  $\mu\text{m}$ , allowing the hydrogen concentration to saturate following the hydrostatic stress state (Fig. 13 in Paper V). Hence, the modelling results are in line with Ref. [165], where lowering the test speed caused an earlier failure.

## 5.4 Recommendations for further research

This thesis identifies several factors that affect the transition temperatures  $T_0$ ,  $T_{28J}$ , and the  $T_0 - T_{28J}$  correlation, but a quantitative physical description has still not been reached. For engineering applications, the accomplishments could prove sufficient. Still, strain-hardening, strain-rate sensitivity, and their temperature dependencies should definitely be further investigated for the ultra-high-strength steels. This could be conducted with digital image correlation measurements to capture the local deformation in tensile tests.

The evaluation of the Master Curve temperature dependency bases on only a few ultra-high-strength materials, so it should be studied with more large data sets (> 20 pcs).

The model proposed in Paper III is very effective, but simple in a few aspects. Given the initial promising results, further research is needed to validate the model for other steel types and test specimen types. Aspects that should be considered are the yield strength coefficient (does it unify the results with different microstructures and lower yield strengths?) and the incorporation of a stress concentration factor to take the notch into account and to apply to fracture toughness specimens. The {100} plane fraction is easy to apply as such, but it is not necessarily the best or most appropriate way to incorporate the size of the continuous local brittle fractures or the toughness-increasing fraction of the ductile canvases separating them.

As segregation bands with very fine prior austenite grain structure are beneficial for the low-temperature toughness, possibilities to produce highly laminar materials with controlled “clean” and strong microsegregation void from large inclusions is a wild possibility worth investigating – assuming that the very fine average effective coarse grain size is easier to achieve than with uniform grain size. From a more conventional perspective, the means to achieve maximum austenite pancaking and minimum hydrogen content should anyhow receive top priority when aiming for the toughest as-quenched materials. The incorporation of hydrogen trapping alloy carbides to the as-quenched materials in question will be beneficial considering the minimization of the diffusible hydrogen.

The HE experiments covered only very narrow test conditions. The temperature range of  $-20\text{ °C}$  and  $-40\text{ °C}$  can be sufficient considering the toughness transition temperatures, but to get an overall picture of low-temperature hydrogen embrittlement, lower strain rates and a higher range of hydrogen contents definitely need to be studied. Also, the same materials should be tested at room temperature to see the effects of hydrogen at the conventional temperature,

although with essentially ductile behaviour. As trapped hydrogen can play a role with HEDE in trap-dense microstructures, quantifying the effects of both trapped and diffusible hydrogen should be interesting. This could be done with both trap-dense and trap-free materials supported by CZM with both quantities incorporated.



## 6 Summary and conclusions

This research focused on three aspects of the ductile-brittle transition temperature toughness properties of as-quenched fully and partially martensitic low-carbon steels: 1) the  $T_0 - T_{28J}$  correlation, 2) microstructural features governing the brittle fracture toughness at these transition temperatures, and 3) hydrogen embrittlement. Data comprised of test data from collaborators and 19 steels produced by laboratory hot-rolling and heat treatments. Standardised toughness tests are accompanied by microstructural and fractographic characterisation, and by cohesive zone modelling. The aim was to provide up-to-date understanding about the fracture mechanical behaviour of this group of ultra-high-strength steels under different environmental conditions, identify their weakest links, and to propose suitable tools for the implementation of these steels in standards standardisation that have so far completely omitted them. The main results and conclusions are as follows:

- For as-quenched low-carbon steels, the relationship between the fracture toughness reference temperature  $T_0$  and the impact toughness transition temperature  $T_{28J}$  cannot be described by previously available correlations. With as-quenched materials,  $T_0$  is higher than  $T_{28J}$ . The only exception to this observation was found in the case of a single centreline plate with excessive splitting in the fracture toughness specimens. A new  $T_0 - T_{28J}$  correlation, specific to the studied steels and hardened welds, has been proposed to allow better estimates of  $T_0$  to be made on the basis of known  $T_{28J}$  values.
- The as-quenched materials can possess equally good transition temperatures ( $T_0$  or  $T_{28J}$ ) to quenched and tempered materials, but  $T_0 > T_{28J}$  rather than the opposite. This difference can be due to 1) the higher “true” microscopic yield strength of as-quenched materials, 2) the difference in the hydrogen contents which will tend to be lower in high-temperature tempered Q&T materials, and 3) differing strain-hardening properties.
- Overall, the Master Curve is capable of describing the ultra-high strength steels with yield strengths of 900 MPa and over. Its accuracy increases for these steels with slightly lower coefficient of the temperature dependency. A general  $T_0 - T_{28J}$  correlation that corrects the magnitude of the effects of yield strength and upper shelf toughness can be used regardless of the strength or quality of ferritic steels.
- The investigated direct-quenched ultra-high-strength steels can possess good low-temperature toughness, generally down to  $T_{28J}$  of  $-120$  °C and  $T_0$  of -

100 °C, making them potential candidates for structural use also in cold regions. The crucial part in the production of these steels is the control of the coarse grain size and the size of the largest brittle inclusions, which correspond to the effective grain size at 80% to 90% in the cumulative grain size distribution. The most efficient way to reduce the size of the coarsest grains and the {100} cleavage planes is to apply generous austenite pancaking, i.e. reduction of the prior austenite grains below the recrystallisation stop temperature. A mixture of martensite and lower and/or upper bainite yields the best combination of toughness and strength within the studied cases. The used process methods left the effective coarse grain size of fully martensitic steels too large for them to achieve very low transition temperatures. The formation of granular bainite impairs the toughness properties as it coarsens the effective grain size.

- A dynamic reference toughness  $K_{I,d,ref}$ , originally introduced in Paper III, links to the propagation of a local Griffith crack using a room-temperature dynamic yield stress and the effective coarse grain size. It has a very close correlation with the impact toughness transition temperatures – with decreasing temperature (of a given level of energy absorption) the reference toughness level “needed” for the crack propagation decreases. To improve toughness of a given strength level, the coarse particle size must be refined. Based on fractography, this consideration can be extended to inclusions.
- Combining the dynamic reference toughness with the fraction of {100} cleavage planes within  $\pm 15^\circ$  of the notch/crack plane allows an accurate estimation of the impact transition temperatures based on a simple semi-physical model consisting of just two parameters.
- Local inhomogeneity can lead to improvement in fracture toughness and  $T_0$  even though the impact toughness,  $T_{28J}$ , and tensile properties would have only insignificant changes. This is due to drastically smaller prior austenite grain size within the segregation bands that cause 43% smaller effective coarse grain size for the centreline material when compared to the homogeneous “clean” material cut above it from the same continuously cast bloom. This improvement in  $d_{ecgs}$  is more than enough to compensate for the high-hardness centreline, both macroscopically and within the segregation bands, and the high frequency of large inclusions in the middle third of its thickness.
- The fracture toughness of the inhomogeneous “dirty” segregated and inclusion-rich material improves by the lowered probability to encounter a coarse cleavage crack nucleating inclusion that is surrounded by coarse grains within the central part of the crack front, which is the failure criterion based on the

fractographic evidence. Present small splits in the inhomogeneous centreline material increase the measured toughness without causing invalid results. Large MnS inclusions promote splitting, but large brittle TiN and CaOS based inclusions are the ones nucleating the failure.

- In contrast to the general hypothesis that hydrogen would not cause problems at temperatures below zero degrees Celsius, hydrogen embrittlement is present and can lower the quasi-static fracture toughness at the ductile-brittle transition temperatures tested and modelled at  $-20\text{ }^{\circ}\text{C}$  and  $-40\text{ }^{\circ}\text{C}$ . This conclusion is consistent with hydrogen-enhanced decohesion theory throughout the study methods, which show that specimens with higher hydrogen content have a slightly lower fracture toughness with significant changes in  $T_0$ , lower plastic deformation under the fracture surfaces, and by the three-step cohesive zone modelling that predicts an even higher decrease in toughness. Allowing for only a fraction of the total hydrogen to be diffusible brings the decrease in toughness in line with the experiments. A given hydrogen content causes a higher increase in  $T_0$  than in  $T_{28J}$ , so increasing hydrogen content separates the values further from each other. Thus, hydrogen contents need to be kept low even considering low-temperature toughness properties.



## 7 Novel features

To the best knowledge of the author, the following findings are original to this work:

- Definitive analysis showing that previous estimates of  $T_0$  based on  $T_{28J}$  are incapable of describing  $T_0$  for as-quenched (untempered) martensitic and partially martensitic microstructures.
- A new  $T_0 - T_{28J}$  correlation unique to the given microstructural condition.
- An evaluation of the Master Curve method considering ultra-high-strength steels with a statistically sufficient sample size.
- An improved engineering application of the  $T_0 - T_{28J}$  correlation which can estimate the fracture toughness reference temperature  $T_0$  of structural steels, covering the grades and microstructures from the mild strength steels to the ultra-high-strength steels.
- The introduction of a dynamic reference toughness and its application to impact toughness transition temperatures.
- A novel efficient semi-physical model for the estimation of the impact toughness transition temperatures.
- A demonstration of how the traditionally deleterious centreline segregation can lead to improved fracture toughness by introducing a “laminar” fine-grained stretches enclosing the largest inclusions.
- The first published study on hydrogen embrittlement at sub-zero temperatures (the other candidate, the conference abstract of Ref. [25] was presented on 11.–14.9.2016 while Paper V was submitted on 22.8.2016 and published on 3.2.2017).
- Hydrogen embrittlement has been shown to be active even at sub-zero ductile-brittle transition temperatures under standard fracture toughness test conditions.
- An example of hydrogen affecting the  $T_0 - T_{28J}$  correlation.



## References

- [1] World Steel Association, World Steel in Figures, (2017) 31.
- [2] S.M. Lensink, Capacity Building for Sustainable Transport: Optimizing the the Energy Use of Traffic and Infrastructure, (2005).
- [3] J.-P. Birat, J.-P. Vizios, Y. de Lassat de Pressigny, M. Schneider, M. Jeanneau, CO<sub>2</sub> Emissions and the Steel Industry's available Responses to the Greenhouse Effect, in: Abat. Greenh. Gas Emiss. Metall. Mater. Process Ind., San Diego, 1999: p. 19.
- [4] Enhancing the EU's industrial competitiveness through the EU ETS innovation fund HYBRIT – A Swedish prefeasibility study project for hydrogen based CO<sub>2</sub>-free ironmaking, (2016).
- [5] European Commission - Joint Research Centre, EN 1993: Design of steel structures, (2017).
- [6] J. Kömi, P. Karjalainen, D. Porter, Direct-Quenched Structural Steels, in: *Encycl. Iron, Steel, Their Alloy.*, CRC Press, 2016: pp. 1109–1125. doi:10.1081/E-EISA-120049737.
- [7] European Commission, EUR-Lex - 32015L0719 - EUR-Lex, Doc. 32015L0719. (n.d.).
- [8] P. Nevasmaa, P. Karjalainen-Roikonen, A. Laukkanen, T. Nykänen, A. Ameri, T. Björk, T. Limmell, J. Kuoppala, Fracture characteristics of new ultra- high-strength steel with yield strengths 900 - 960 MPa, in: 2nd Int. Conf. Super-High Strength Steels, Associazione Italiana di Metallurgia, Verona, Italy, 2010.
- [9] A.J. Kaijalainen, P.P. Suikkanen, T.J. Limmell, L.P. Karjalainen, J.I. Kömi, D.A. Porter, Effect of austenite grain structure on the strength and toughness of direct-quenched martensite, *J. Alloys Compd.* 577 (2013) S642–S648. doi:10.1016/j.jallcom.2012.03.030.
- [10] ASTM International, E1921-14a: Standard Test Method for Determination of Reference Temperature, T<sub>0</sub>, for ferritic Steels in the Transition Range, 2015. doi:10.1520/E1921-05.
- [11] K. Wallin, A Simple Theoretical Charpy V - KIC Correlation for Irradiation Embrittlement. Innovative Approaches to Irradiation Damage and Fracture Analysis, in: PVP 170, ASME, 1989: pp. 93–100.
- [12] CEN, EN 1993-1-12, Eurocode 3, Design of steel structures - Part 1-12: Additional rules for the extension of EN 1993 up to steel grades S 700, CEN - European Committee for Standardization, 2007.
- [13] SINTAP, Structural Integrity Assessment Procedures for European Industry - Final Procedure, Report No. BE95-1426/FR/7, 1999.
- [14] FITNET, FITNET Fitness-for-Service (FFS) – Procedure (Volume I), Revision M, European Thematic Network FITNET, Geesthacht, 2008.
- [15] K. Wallin, The master curve method: a new concept for brittle fracture, *Int. J. Mater. Prod. Technol.* 14 (1999) 342. doi:10.1504/IJMPT.1999.036276.
- [16] C. Berdin, J. Besson, S. Bugat, R. Desmorat, F. Feyel, S. Forest, E. Lorentz, E. Maire, T. Pardoen, A. Pineau, B. Tanguy, Local Approach to Fracture, 2004.
- [17] F.M. Beremin, A Local Criterion for Cleavage Fracture of a Nuclear Pressure Vessel Steel, *Metall. Mater. Trans. A.* 14A (1983) 2277–2287.

- [18] CEN, EN 1993-1-10, Eurocode 3, Design of steel structures - Part 1-10: Material toughness and through-thickness properties, 2005.
- [19] K. Wallin, Fracture Toughness of Engineering Materials - Estimation and Application, EMAS Publishing, Warrington, 2011.
- [20] CEN, EN 13001-3-1:2012+A1, Cranes -General Design -Part 3-1: Limit States and proof competence of steel structure, 2013.
- [21] F.B. Pickering, T. Gladman, Metallurgical developments in carbon steels, Iron Steel Inst. Spec. Rep. 81 (1963) 10–25.
- [22] B. Mintz, G. Peterson, A. Nassar, Structure-property relationships in ferrite-pearlite steels, Ironmak. Steelmak. 21 (1994) 215–222.
- [23] W.H. Johnson, On some remarkable change produced in iron and steel by the action of hydrogen and acids, Proc. R. Soc. London. 23 (1875) 168–179.
- [24] A. Nagao, M. Dadfarnia, B.P. Somerday, P. Sofronis, R.O. Ritchie, Hydrogen-enhanced-plasticity mediated decohesion for hydrogen-induced intergranular and “quasi-cleavage” fracture of lath martensitic steels, J. Mech. Phys. Solids. 112 (2018) 403–430. doi:10.1016/j.jmps.2017.12.016.
- [25] Y. Momotani, A. Shibata, N. Tsuji, Effect of Deformation Temperature on Hydrogen Embrittlement in Low-Carbon Martensitic Steel, in: Int. Hydrog. Conf. (IHC 2016) Mater. Perform. Hydrog. Environ., ASME Press, n.d. doi:10.1115/1.861387\_ch9.
- [26] C. Ouchi, Development of Steel Plates by Intensive Use of TMCP and Direct Quenching Processes, ISIJ Int. 41 (2001) 542–553.
- [27] M. Espenhahn, T. Heller, J. Esdohr, Hot-rolled steel strip and method of making it, WO1998002589, 1998.
- [28] M.P. Hemmilä, R.A. Liimatainen, T.P. Liimatainen, Hot-rolled Steel Strip and Method for Manufacturing the Same, EP1375694, 2004.
- [29] D.A. Porter, K.E. Easterling, M.Y. Sherif, Phase transformations in metals and alloys, 3rd ed., CRC Press, 2009.
- [30] H.K.D.H. Bhadeshia, R.W.K. Honeycombe, Steels - Microstructure and Properties, 3rd ed., Elsevier, Oxford, 2006.
- [31] K.-E. Thelning, Bofors Handbok - Värmebehandling av Stål, Karlebo & AB Bofors, 1976.
- [32] D. Lohe, O. Vohringer, Stability of residual stresses, Handb. Residual Stress Deform. Steel. (2002) 54–69. doi:10.1361/hrsd2002p054.
- [33] B. Hutchinson, D. Lindell, M. Barnett, Yielding Behaviour of Martensite in Steel, ISIJ Int. 55 (2015) 1114–1122. doi:10.2355/isijinternational.55.1114.
- [34] B. Hutchinson, A. Bengtson, Hydrogen in Steels – a Literature Study, Swedish Inst. Met. Res. Report No: (2002).
- [35] S.-J. Lee, J.A. Ronevich, G. Krauss, D.K. Matlock, Hydrogen Embrittlement of Hardened Low-carbon Sheet Steel, ISIJ Int. 50 (2010) 294–301. doi:10.2355/isijinternational.50.294.

- [36] A. Shibata, T. Murata, H. Takahashi, T. Matsuoka, N. Tsuji, Characterization of Hydrogen-Related Fracture Behavior in As-Quenched Low-Carbon Martensitic Steel and Tempered Medium-Carbon Martensitic Steel, *Metall. Mater. Trans. A Phys. Metall. Mater. Sci.* 46 (2015) 5685–5696. doi:10.1007/s11661-015-3176-x.
- [37] B. Hutchinson, J. Hagström, O. Karlsson, D. Lindell, M. Tornberg, F. Lindberg, M. Thuvander, Microstructures and hardness of as-quenched martensites (0.1–0.5%C), *Acta Mater.* 59 (2011) 5845–5858. doi:10.1016/j.actamat.2011.05.061.
- [38] S. Morito, K. Oh-Ishi, K. Hono, T. Ohba, Carbon Enrichment in Retained Austenite Films in Low Carbon Lath Martensite Steel, *ISIJ Int.* 51 (2011) 1200–1202.
- [39] L. Morsdorf, O. Jeannin, D. Barbier, M. Mitsuhara, D. Raabe, C.C.C. Tasan, Multiple mechanisms of lath martensite plasticity, *Acta Mater.* 121 (2016) 202–214.
- [40] S. Morito, H. Tanaka, R. Konishi, T. Furuhashi, T. Maki, The morphology and crystallography of lath martensite in Fe-C alloys, *Acta Mater.* 51 (2003) 1789–1799. doi:10.1016/S1359-6454(02)00577-3.
- [41] F. Maresca, V.G. Kouznetsova, M.G.D. Geers, Subgrain lath martensite mechanics: A numerical-experimental analysis, *J. Mech. Phys. Solids.* 73 (2014) 69–83. doi:10.1016/j.jmps.2014.09.002.
- [42] L. Morsdorf, C.C. Tasan, D. Ponge, D. Raabe, 3D structural and atomic-scale analysis of lath martensite: Effect of the transformation sequence, *Acta Mater.* 95 (2015) 366–377. doi:10.1016/j.actamat.2015.05.023.
- [43] S. Morito, X. Huang, T. Furuhashi, T. Maki, N. Hansen, The morphology and crystallography of lath martensite in alloy steels, *Acta Mater.* 54 (2006) 5323–5331. doi:10.1016/j.actamat.2006.07.009.
- [44] H.K.D.H. Bhadeshia, *Bainite in steels: transformations, microstructure and properties*, 2nd ed., IOM Communications Ltd, London, 2001.
- [45] F.G. Caballero, H. Roelofs, S. Hasler, C. Capdevila, J. Chao, J. Cornide, C. Garcia-Mateo, Influence of bainite morphology on impact toughness of continuously cooled cementite free bainitic steels, *Mater. Sci. Technol.* 28 (2012) 95–102. doi:10.1179/1743284710Y.0000000047.
- [46] H.K. Sung, S.Y. Shin, B. Hwang, C.G. Lee, S. Lee, Effects of B and Cu Addition and Cooling Rate on Microstructure and Mechanical Properties in Low-Carbon, High-Strength Bainitic Steels, *Metall. Mater. Trans. A.* 43 (2012) 3703–3714. doi:10.1007/s11661-012-1183-8.
- [47] S. Zajac, V. Schwinn, K. Tacke, Characterisation and Quantification of Complex Bainitic Microstructures in High and Ultra-High Strength Linepipe Steels, *Mater. Sci. Forum.* 500–501 (2005) 387–394. doi:10.4028/www.scientific.net/MSF.500-501.387.
- [48] T. Furuhashi, H. Kawata, S. Morito, T. Maki, Crystallography of upper bainite in Fe–Ni–C alloys, *Mater. Sci. Eng. A.* 431 (2006) 228–236. doi:10.1016/j.msea.2006.06.032.
- [49] T.L. Anderson, *Fracture mechanics: fundamentals and applications*, Taylor & Francis, 2005.
- [50] ASTM International, E23 – 07: Standard Test Methods for Notched Bar Impact Testing of Metallic Materials, 2007. doi:10.1520/E0023.

- [51] CEN, EN 10045-1: Metallic materials — Charpy impact test — Part 1 □: Test method, 1990.
- [52] ISO, EN ISO 148-1: Metallic Materials, Charpy pendulum impact test, Part 1: Test method, 2009.
- [53] W. Oldfield, Curve fitting impact test data: a statistical procedure, *ASTM Stand. News.* 3 (1975) 24–29.
- [54] J.W. Hutchinson, Singular behaviour at the end of a tensile crack in a hardening material, *J. Mech. Phys. Solids.* 16 (1968).
- [55] J.R. Rice, G.F. Rosengren, Plane strain deformation near a crack tip in a power-law hardening material, *J. Mech. Phys. Solids.* 16 (1968) 1–12. doi:10.1016/0022-5096(68)90013-6.
- [56] J.R. Rice, A Path Independent Integral and the Approximate Analysis of Strain Concentration by Notches and Cracks, *J. Appl. Mech.* 35 (1968) 379. doi:10.1115/1.3601206.
- [57] ASTM International, E1820-13: Standard Test Method for Measurement of Fracture Toughness, 2013. doi:10.1520/E1820-13.Copyright.
- [58] J. Barsom, Rolfe ST, Correlations between KIC and Charpy V-notch test results in the transition–temperature range, in: *Impact Test. Met. ASTM STP 466*, American Society for Testing and Materials, Philadelphia, 1970: pp. 281–302.
- [59] R.H. Sailors, H.T. Corten, Relationship between material fracture toughness using fracture mechanics and transition temperature tests, in: *Proc. 1971 Natl. Symp. Fract. Mech. Part II (ASTM STP 514)*, American Society for Testing and Materials, Philadelphia, 1972: pp. 164–191.
- [60] B. Marandet, G. Sanz, Evaluation of the Toughness of Thick Medium-Strength Steels by Using Linear-Elastic Fracture Mechanics and Correlations Between KIC and Charpy V-Notch, in: *Flaw Growth Fract.*, American Society for Testing and Materials, Philadelphia, 1977: pp. 72–95.
- [61] R. Roberts, C. Newton, Interpretive report on small-scale test correlations with KIC data, *Welding Research Council*, New York, 1981.
- [62] M.A. Sokolov, R.K. Nanstad, Comparison of Irradiation-Induced Shifts of  $K_{Jc}$  and Charpy Impact Toughness for Reactor Pressure Vessel Steels (NUREG/CR-6609), Washington, 2000.
- [63] CEN, Eurocode 3 - Design of steel structures - Part 1-12: Additional rules for the extension of EN 1993 up to steel grades S 700, CEN - European Committee for Standardization, 2007.
- [64] P. Bowen, S.G. Druce, J.F. Knott, Micromechanical modelling of fracture toughness, *Acta Metall.* 35 (1987) 1735–1746. doi:10.1016/0001-6160(87)90119-2.
- [65] X.Z. Zhang, J.F. Knott, Cleavage fracture in bainitic and martensitic microstructures, *Acta Mater.* 47 (1999) 3483–3495. doi:10.1016/S1359-6454(99)00200-1.
- [66] S. Lee, S. Kim, B. Hwang, B.S. Lee, C.G. Lee, Effect of carbide distribution on the fracture toughness in the transition temperature region of an SA 508 steel, *Acta Mater.* 50 (2002) 4755–4762. doi:10.1016/S1359-6454(02)00313-0.

- [67] K. Wallin, A. Laukkanen, New developments of the Wallin, Saario, Törrönen cleavage fracture model, *Eng. Fract. Mech.* 75 (2008) 3367–3377. doi:10.1016/j.engfracmech.2007.07.018.
- [68] H. C. H.C., The Importance of the Non-Metallic Inclusions in Steel, *Nature*. 101 (1918) 334–335.
- [69] P. Bowen, J.F. Knott, Cleavage fracture of A 533 B pressure vessel steel in martensitic condition, *Met. Sci.* 18 (1984) 225–235. doi:10.1179/030634584790420131.
- [70] M. Mäntylä, A. Rossoll, I. Nedbal, C. Prioul, B. Marini, Fractographic observations of cleavage fracture initiation in a bainitic A508 steel, *J. Nucl. Mater.* 264 (1999) 257–262. doi:10.1016/S0022-3115(98)00496-6.
- [71] A. Echeverría, J.M. Rodríguez-Ibabe, Brittle fracture micromechanisms in bainitic and martensitic microstructures in a C-Mn-B steel, *Scr. Mater.* 41 (1999) 131–136. doi:10.1016/S1359-6462(99)00124-4.
- [72] W.W. Bose Filho, A.L.M. Carvalho, P. Bowen, Micromechanisms of cleavage fracture initiation from inclusions in ferritic welds Part II. Quantification of local fracture behaviour observed in fatigue pre-cracked testpieces, *Mater. Sci. Eng. A.* 452–453 (2007) 401–410. doi:10.1016/j.msea.2007.01.115.
- [73] W.W. Bose Filho, A.L.M. Carvalho, P. Bowen, Micromechanisms of cleavage fracture initiation from inclusions in ferritic welds. Part I. Quantification of local fracture behaviour observed in notched testpieces, *Mater. Sci. Eng. A.* 460–461 (2007) 436–452. doi:10.1016/j.msea.2007.01.115.
- [74] B. Tanguy, J. Besson, R. Piques, A. Pineau, Ductile to brittle transition of an A508 steel characterized by Charpy impact test Part I: experimental results, *Eng. Fract. Mech.* 72 (2005) 49–72. doi:10.1016/j.engfracmech.2004.03.010.
- [75] W. Barr, C. Tipper, Brittle fracture in mild-steel plates, *J. Iron Steel Inst.* 157 (1947) 223.
- [76] T. Hanamura, F. Yin, K. Nagai, Ductile-Brittle Transition Temperature of Ultrafine Ferrite/Cementite Microstructure in a Low Carbon Steel Controlled by Effective Grain Size, *ISIJ Int.* 44 (2004) 610–617. doi:10.2355/isijinternational.44.610.
- [77] A. Lambert-Perlade, A.F. Gourgues, J. Besson, T. Sturel, A. Pineau, Mechanisms and modeling of cleavage fracture in simulated heat-affected zone microstructures of a high-strength low alloy steel, *Metall. Mater. Trans. A.* 35 (2004) 1039–1053. doi:10.1007/s11661-004-1007-6.
- [78] D. Bhattacharjee, J.F. Knott, C.L. Davis, Charpy-impact-toughness prediction using an “effective” grain size for thermomechanically controlled rolled microalloyed steels, *Metall. Mater. Trans. A.* 35 (2004) 121–130. doi:10.1007/s11661-004-0115-7.
- [79] C. Wang, M. Wang, J. Shi, W. Hui, H. Dong, Effect of microstructural refinement on the toughness of low carbon martensitic steel, *Scr. Mater.* 58 (2008) 492–495. doi:10.1016/j.scriptamat.2007.10.053.
- [80] B. Hwang, C.G. Lee, T.-H. Lee, Correlation of Microstructure and Mechanical Properties of Thermomechanically Processed Low-Carbon Steels Containing Boron and Copper, *Metall. Mater. Trans. A.* 41 (2010) 85–96. doi:10.1007/s11661-009-0070-4.

- [81] B. Hwang, C.G. Lee, S.-J. Kim, Low-Temperature Toughening Mechanism in Thermomechanically Processed High-Strength Low-Alloy Steels, *Metall. Mater. Trans. A.* 42 (2011) 717–728. doi:10.1007/s11661-010-0448-3.
- [82] J.W. Morris, Jr., On the Ductile-Brittle Transition in Lath Martensitic Steel, *ISIJ Int.* 51 (2011) 1569–1575. doi:10.2355/isijinternational.51.1569.
- [83] I. Gutiérrez, Effect of microstructure on the impact toughness of Nb-microalloyed steel: Generalisation of existing relations from ferrite–pearlite to high strength microstructures, *Mater. Sci. Eng. A.* 571 (2013) 57–67. doi:10.1016/j.msea.2013.02.006.
- [84] J.W. Morris, C. Kinney, K. Pytlewski, Y. Adachi, Microstructure and cleavage in lath martensitic steels, *Sci. Technol. Adv. Mater.* 14 (2013) 14208. doi:10.1088/1468-6996/14/1/014208.
- [85] N. Isasti, D. Jorge-Badiola, M.L. Taheri, P. Uranga, Microstructural Features Controlling Mechanical Properties in Nb-Mo Microalloyed Steels. Part II: Impact Toughness, *Metall. Mater. Trans. A.* 45 (2014) 4972–4982. doi:10.1007/s11661-014-2451-6.
- [86] H. Terasaki, Y. Miyahara, M. Ohata, K. Moriguchi, Y. Tomio, K. Hayashi, Visualization of Microstructural Factor Resisting the Cleavage-Crack Propagation in the Simulated Heat-Affected Zone of Bainitic Steel, *Metall. Mater. Trans. A.* 46 (2015) 5489–5493. doi:10.1007/s11661-015-3167-y.
- [87] T. Jia, Y. Zhou, X. Jia, Z. Wang, Effects of Microstructure on CVN Impact Toughness in Thermomechanically Processed High Strength Microalloyed Steel, *Metall. Mater. Trans. A.* 48 (2016) 685–696. doi:10.1007/s11661-016-3893-9.
- [88] J. Han, A.K. da Silva, D. Ponge, D. Raabe, S.-M. Lee, Y.-K. Lee, S.-I. Lee, B. Hwang, The effects of prior austenite grain boundaries and microstructural morphology on the impact toughness of intercritically annealed medium Mn steel, *Acta Mater.* 122 (2017) 199–206. doi:10.1016/j.actamat.2016.09.048.
- [89] J. Du, M. Strangwood, C.L. Davis, Effect of TiN Particles and Grain Size on the Charpy Impact Transition Temperature in Steels, *J. Mater. Sci. Technol.* 28 (2012) 878–888. doi:10.1016/S1005-0302(12)60146-7.
- [90] A. Ghosh, A. Ray, D. Chakrabarti, C.L. Davis, Cleavage initiation in steel: Competition between large grains and large particles, *Mater. Sci. Eng. A.* 561 (2013) 126–135. doi:10.1016/j.msea.2012.11.019.
- [91] R. Cao, G. Li, X.Y. Fang, J. Song, J.H. Chen, Investigation on the effects of microstructure on the impact and fracture toughness of a C-Mn steel with various microstructures, *Mater. Sci. Eng. A.* 564 (2013) 509–524. doi:10.1016/j.msea.2012.11.120.
- [92] Z. Guo, C.S. Lee, J.W. Morris, On coherent transformations in steel, (2004). doi:10.1016/j.actamat.2004.08.011.
- [93] P. Lehto, H. Remes, T. Saukkonen, H. Hänninen, J. Romanoff, Influence of grain size distribution on the Hall-Petch relationship of welded structural steel, *Mater. Sci. Eng. A.* 592 (2014) 28–39. doi:10.1016/j.msea.2013.10.094.

- [94] S. Pallaspuuro, A. Kaijalainen, T. Limnell, D.A. Porter, Tempering of direct quenched low-alloy ultra-high-strength steel, Part II - Mechanical properties, in: *Adv. Mater. Res.*, 2014: pp. 580–585. doi:10.4028/www.scientific.net/AMR.922.580.
- [95] J. Hannula, J. Kömi, D.A. Porter, M.C. Somani, A. Kaijalainen, P. Suikkanen, J.-R. Yang, S.-P. Tsai, Effect of Boron on the Strength and Toughness of Direct-Quenched Low-Carbon Niobium Bearing Ultra-High-Strength Martensitic Steel, *Metall. Mater. Trans. A*. (2017) 1–13. doi:10.1007/s11661-017-4295-3.
- [96] P. Yan, O.E. Güngör, P. Thibaux, M. Liebeherr, H.K.D.H. Bhadeshia, Tackling the toughness of steel pipes produced by high frequency induction welding and heat-treatment, *Mater. Sci. Eng. A*. 528 (2011) 8492–8499. doi:10.1016/j.msea.2011.07.034.
- [97] M.S. Joo, D.-W. Suh, J.H. Bae, H.K.D.H. Bhadeshia, Role of delamination and crystallography on anisotropy of Charpy toughness in API-X80 steel, *Mater. Sci. Eng. A*. 546 (2012) 314–322. doi:10.1016/J.MSEA.2012.03.079.
- [98] C. Zong, G. Zhu, W. Mao, Effect of crystallographic texture on the anisotropy of Charpy impact behavior in pipeline steel, *Mater. Sci. Eng. A*. 563 (2013) 1–7. doi:10.1016/J.MSEA.2012.11.055.
- [99] X.-L. Yang, Y.-B. Xu, X.-D. Tan, D. Wu, Influences of crystallography and delamination on anisotropy of Charpy impact toughness in API X100 pipeline steel, *Mater. Sci. Eng. A*. 607 (2014) 53–62. doi:10.1016/J.MSEA.2014.03.121.
- [100] S. Pillot, P. Pacqueau, An attempt to define a Charpy V-notched mastercurve to fit transition of ferritic steels, *Eng. Fract. Mech.* 135 (2015) 259–273. doi:10.1016/j.engfracmech.2015.01.012.
- [101] Y. Tomita, Improved fracture toughness of ultrahigh strength steel through control of non-metallic inclusions, *J. Mater. Sci.* 28 (1993) 853–859. doi:10.1007/BF00400864.
- [102] K. Wallin, M. Yamamoto, U. Ehrnstén, Location of initiation sites in fracture toughness testing specimen - The effect of size and side grooves, in: *Proc. ASME 2016 Press. Vessel. Pip. Conf.*, ASME, Vancouver, 2016: pp. 1–9.
- [103] Z. Sterjovski, D.P. Dunne, D.G. Carr, S. Ambrose, The Effect of Cold Work and Fracture Surface Splitting on the Charpy Impact Toughness of Quenched and Tempered Steels, *ISIJ Int.* 44 (2004) 1114–1120.
- [104] R. Punch, M. Strangwood, C. Davis, Origin and propagation of splits in high-strength low-alloy strip steel, *Metall. Mater. Trans. A Phys. Metall. Mater. Sci.* 43 (2012) 4622–4632. doi:10.1007/s11661-012-1307-1.
- [105] X.J. Shen, S. Tang, Y.J. Wu, X.L. Yang, J. Chen, Z.Y. Liu, R.D.K. Misra, G.D. Wang, Evolution of microstructure and crystallographic texture of microalloyed steel during warm rolling in dual phase region and their influence on mechanical properties, *Mater. Sci. Eng. A*. 685 (2017) 194–204. doi:10.1016/J.MSEA.2016.12.108.
- [106] M. Yang, Y.J. Chao, X. Li, D. Immel, J. Tan, Splitting in dual-phase 590 high strength steel plates Part II. Quantitative analysis and its effect on Charpy impact energy, *Mater. Sci. Eng. A*. 497 (2008) 462–470.
- [107] E. Maina, D.N. Crowther, J.R. Banerjee, B. Mintz, Influence of directionality on strength and impact behaviour of high strength steels, *Mater. Sci. Technol.* 28 (2012) 390–396. doi:10.1179/1743284711Y.0000000061.

- [108] C.D. Beachem, A new model for hydrogen-assisted cracking (hydrogen “embrittlement”), *Metall. Trans.* 3 (1972) 441–455. doi:10.1007/BF02642048.
- [109] H.K. Birnbaum, P. Sofronis, Hydrogen-enhanced localized plasticity—a mechanism for hydrogen-related fracture, *Mater. Sci. Eng. A.* 176 (1994) 191–202. doi:10.1016/0921-5093(94)90975-X.
- [110] R.A. Oriani, A mechanistic theory of hydrogen embrittlement of steels, *Berichte Der Bunsengesellschaft Für Phys. Chemie.* 76 (1972) 848–857. doi:10.1002/bbpc.19720760864.
- [111] Y.-H. Kim, H.J. Kim, J.W. Morris, The influence of precipitated austenite on hydrogen embrittlement in 5.5Ni steel, *Metall. Trans. A.* 17 (1986) 1157–1164. doi:10.1007/BF02665314.
- [112] M. Wang, E. Akiyama, K. Tsuzaki, Hydrogen degradation of a boron-bearing steel with 1050 and 1300MPa strength levels, *Scr. Mater.* 52 (2005) 403–408. doi:10.1016/j.scriptamat.2004.10.023.
- [113] A. Nagao, C.D. Smith, M. Dadfarnia, P. Sofronis, I.M. Robertson, The role of hydrogen in hydrogen embrittlement fracture of lath martensitic steel, *Acta Mater.* 60 (2012) 5182–5189. doi:10.1016/j.actamat.2012.06.040.
- [114] A. Nagao, C.D. Smith, M. Dadfarnia, P. Sofronis, I.M. Robertson, Interpretation of Hydrogen-induced Fracture Surface Morphologies for Lath Martensitic Steel, *Procedia Mater. Sci.* 3 (2014) 1700–1705. doi:10.1016/j.mspro.2014.06.274.
- [115] A. Shibata, H. Takahashi, N. Tsuji, Microstructural and Crystallographic Features of Hydrogen-related Crack Propagation in Low Carbon Martensitic Steel, *ISIJ Int.* 52 (2012) 208–212. doi:10.2355/isijinternational.52.208.
- [116] C.J. McMahon, Hydrogen-induced intergranular fracture of steels, *Eng. Fract. Mech.* 68 (2001) 773–788. doi:10.1016/S0013-7944(00)00124-7.
- [117] M.L. Martin, J.A. Fenske, G.S. Liu, P. Sofronis, I.M. Robertson, On the formation and nature of quasi-cleavage fracture surfaces in hydrogen embrittled steels, *Acta Mater.* 59 (2011) 1601–1606. doi:10.1016/j.actamat.2010.11.024.
- [118] M.L. Martin, I.M. Robertson, P. Sofronis, Interpreting hydrogen-induced fracture surfaces in terms of deformation processes: A new approach, *Acta Mater.* 59 (2011) 3680–3687. doi:10.1016/j.actamat.2011.03.002.
- [119] A. Laureys, T. Depover, R. Petrov, K. Verbeken, Microstructural characterization of hydrogen induced cracking in TRIP-assisted steel by EBSD, *Mater. Charact.* 112 (2016) 169–179. doi:10.1016/j.matchar.2015.12.017.
- [120] S.I. Wright, M.M. Nowell, D.P. Field, A Review of Strain Analysis Using Electron Backscatter Diffraction, *Microsc. Microanal.* 17 (2011) 316–329. doi:10.1017/S1431927611000055.
- [121] S. Matsuoka, STX-21 Project report, (2002).
- [122] V. Olden, A. Alvaro, O.M. Akselsen, Hydrogen diffusion and hydrogen influenced critical stress intensity in an API X70 pipeline steel welded joint – Experiments and FE simulations, *Int. J. Hydrogen Energy.* 37 (2012) 11474–11486. doi:10.1016/j.ijhydene.2012.05.005.

- [123] M. Tvrđy, V. Suchanek, L. Hyspecka, K. Mazanek, Effect of metallurgy on stress corrosion cracking and hydrogen embrittlement of ultrahigh strength steels, in: D. Taplin (Ed.), *Adv. Res. Strength Fract. Mater. 4th Int. Conf. Fract.*, University of Waterloo Press, Waterloo, 1977: pp. 255–59.
- [124] O. Wang, S. Adolfsson, T. Siwecki, Critical Hydrogen Level for Mechanical Property Degradation of High Strength Steels, Swedish Inst. Met. Res. Report No: (2004).
- [125] Wang X.T., T. Siwecki, Study on Susceptibility of Hydrogen Embrittlement in a Tool Steel, *Mater. Sci. Forum.* (2007) 103–106. <http://zh.scientific.net/MSF.561-565.103.pdf> (accessed May 30, 2016).
- [126] V. Olden, C. Thaulow, R. Johnsen, E. Østby, Cohesive zone modeling of hydrogen-induced stress cracking in 25% Cr duplex stainless steel, *Scr. Mater.* 57 (2007) 615–618. doi:10.1016/j.scriptamat.2007.06.006.
- [127] V. Olden, C. Thaulow, R. Johnsen, E. Østby, T. Berstad, Application of hydrogen influenced cohesive laws in the prediction of hydrogen induced stress cracking in 25%Cr duplex stainless steel, *Eng. Fract. Mech.* 75 (2008) 2333–2351. doi:10.1016/j.engfracmech.2007.09.003.
- [128] A. Needleman, Some Issues in Cohesive Surface Modeling, *Procedia IUTAM.* 10 (2014) 221–246. doi:10.1016/j.piutam.2014.01.020.
- [129] H. Yu, J.S. Olsen, A. Alvaro, V. Olden, J. He, Z. Zhang, A uniform hydrogen degradation law for high strength steels, *Eng. Fract. Mech.* 157 (2016) 56–71. doi:10.1016/j.engfracmech.2016.02.001.
- [130] S. Serebrinsky, E. Carter, M. Ortiz, A quantum-mechanically informed continuum model of hydrogen embrittlement, *J. Mech. Phys. Solids.* 52 (2004) 2403–2430. doi:10.1016/j.jmps.2004.02.010.
- [131] A. Kaijalainen, Effect of microstructure on the mechanical properties and bendability of direct-quenched ultrahigh-strength steels, University of Oulu, 2016.
- [132] CEN, EN 10002-1: Metallic materials — Tensile testing — Part 1: Method of test at ambient temperature, 2001.
- [133] ISO, EN ISO 6892-1: Metallic materials, Tensile testing, Part 1: Method of test at room temperature, 2009.
- [134] ASTM International, E1823-13: Standard Terminology Relating to Fatigue and Fracture Testing, 2013. doi:10.1520/E1823-13.2.
- [135] G. Krauss, *Steels - Processing, Structure, and Performance*, 2nd ed., ASM International, Materials Park, 2015.
- [136] R. Blondeau, P. Maynier, J. Dollet, Forecasting the hardness and resistance of carbon and low-alloy steels according to their structure and composition, *Mem. Sci. Rev. Met.* (1973).
- [137] H.B. Mann, D.R. Whitney, On a Test of Whether one of Two Random Variables is Stochastically Larger than the Other, *Ann. Math. Stat.* 18 (1947) 50–60. doi:10.1214/aoms/1177730491.
- [138] V. Olden, C. Thaulow, R. Johnsen, Modelling of hydrogen diffusion and hydrogen induced cracking in supermartensitic and duplex stainless steels, *Mater. Des.* 29 (2008) 1934–1948.

- [139] W.C. Luu, J.K. Wu, The influence of microstructure on hydrogen transport in carbon steels, *Corros. Sci.* 38 (1996) 239–245. doi:10.1016/0010-938X(96)00109-6.
- [140] N. Parvathavarthini, S. Saroja, R.K. Dayal, Influence of microstructure on the hydrogen permeability of 9%Cr–1%Mo ferritic steel, *J. Nucl. Mater.* 264 (1999) 35–47. doi:10.1016/S0022-3115(98)00486-3.
- [141] S.L.I. Chan, Hydrogen trapping ability of steels with different microstructures, *J. Chinese Inst. Eng.* 22 (1999) 43–53. doi:10.1080/02533839.1999.9670440.
- [142] E. Hörnlund, J.K.T. Fossen, S. Hauger, C. Haugen, T. Havn, T. Hemmingsen, T. Hörnlund, E., Fossen, J., Hauger, S., Haugen, C., Havn, T and Hemmingsen, Hydrogen Diffusivities and Concentrations in 520M Carbon Steel under Cathodic Protection in 0.5M NaCl and the Effect of Added Sulphite, Dithionite, Thiosulphate, and Sulphide, *Int. J. Electrochem. Sci.* 2 (2007) 82–92.
- [143] T. Böllinghaus, H. Hoffmeister, C. Middel, Scatterbands for hydrogen diffusion coefficients in steels having a ferritic or martensitic microstructure and steels having an austenitic microstructure at room temperature, *Weld. World.* 1 (1996) 16–23.
- [144] ABAQUS User Manual, Version 6.14-1, Dassault Systemes Simulia Corp., Providence, RI; 2014, (n.d.).
- [145] A. Needleman, A Continuum Model for Void Nucleation by Inclusion Debonding, *J. Appl. Mech.* 54 (1987) 525. doi:10.1115/1.3173064.
- [146] Y.F. Gao, A.F. Bower, A simple technique for avoiding convergence problems in finite element simulations of crack nucleation and growth on cohesive interfaces, *Model. Simul. Mater. Sci. Eng.* 12 (2004) 453–463. doi:10.1088/0965-0393/12/3/007.
- [147] G. Sedlacek, M. Feldmann, B. Kühn, D. Tschickardt, S. Höhler, C. Müller, W. Hensen, N. Stranghöner, W. Dahl, P. Langenberg, S. Münstermann, J. Brozetti, J. Raoul, R. Pope, F. Bijlaard, Commentary and Worked examples to EN 1993-1-10 “Material toughness and through thickness properties” and other toughness oriented rules in EN 1993, 2008.
- [148] T. Nitschke-Pagel, A. Hesse, K. Dilger, Untersuchungen zum Einfluss von Härte- und Gefügestand strahlgeschweißter Verbindungen auf deren Verformungs- und Tragverhalten. Schlussbericht zu IGF-Vorhaben Nr. 18.087 N, Braunschweig, 2017.
- [149] A.-C. Hesse, T. Nitschke-Pagel, K. Dilger, Investigations on the fracture toughness of beam welded structural steels with yield strengths from 355 MPa to 960 MPa, *Int. Inst. Weld.* (2017) 15.
- [150] X.Z. Zhang, J.F. Knott, The statistical modelling of brittle fracture in homogeneous and heterogeneous steel microstructures, *Acta Mater.* 48 (2000) 2135–2146. doi:10.1016/S1359-6454(00)00055-0.
- [151] D. Lohe, K. Lang, O. Vohringer, Residual stresses and fatigue behavior, in: *Handb. Residual Stress Deform. Steel*, 2002: pp. 27–53. doi:10.1361/hrsd2002p027.
- [152] J. Hensel, Einfluss von Schweißeigenspannungen auf den Schwingfestigkeitsnachweis von Schweißverbindungen im Nennspannungskonzept, *Shaker*, 2017.

- [153] A. Kaijalainen, S. Pallaspuuro, D. a. Porter, Tempering of Direct Quenched Low-Alloy Ultra-High-Strength Steel, Part I – Microstructure, in: *Adv. Mater. Res.*, 2014: pp. 316–321. doi:10.4028/www.scientific.net/AMR.922.316.
- [154] A. Saastamoinen, A. Kaijalainen, D. Porter, P. Suikkanen, The effect of thermomechanical treatment and tempering on the subsurface microstructure and bendability of direct-quenched low-carbon strip steel, *Mater. Charact.* 134 (2017) 172–181. doi:10.1016/J.MATCHAR.2017.10.020.
- [155] W.-S. Lee, T.-T. Su, Mechanical properties and microstructural features of AISI 4340 high-strength alloy steel under quenched and tempered conditions, *J. Mater. Process. Technol.* 87 (1999) 198–206.
- [156] Y. Yun, Q. Cai, B. Xie, S. Li, Effect of tempering temperature on strain hardening exponent and flow stress curve of 1000 MPa grade steel for construction machinery, *J. Iron Steel Res. Int.* 24 (2017) 950–956. doi:10.1016/S1006-706X(17)30138-3.
- [157] P.J. Withers, H.K.D.H. Bhadeshia, Residual stress. Part 2 – Nature and origins, *Mater. Sci. Technol.* 17 (2001) 366–375. doi:10.1179/026708301101510087.
- [158] K. Wallin, P. Karjalainen-Roikonen, P. Suikkanen, Extension of EN 1993-1-10 and EN 1993-1-12: To higher strengths and thinner sections, in: *EUROSTEEL 2017*, 2017: p. 10.
- [159] A. Neimitz, I. Dzioba, T. Linnell, Modified master curve of ultra high strength steel, *Int. J. Press. Vessel. Pip.* 92 (2012) 19–26. doi:10.1016/J.IJPVP.2012.01.008.
- [160] J.I. San Martin, J.M. Rodriguez-Ibabe, Determination of energetic parameters controlling cleavage fracture in a Ti-V microalloyed ferrite-pearlite steel, *Scr. Mater.* 40 (1999) 459–464. doi:10.1016/S1359-6462(98)00467-9.
- [161] M. Wang, E. Akiyama, K. Tsuzaki, Effect of hydrogen and stress concentration on the notch tensile strength of AISI 4135 steel, *Mater. Sci. Eng. A.* 398 (2005) 37–46. doi:10.1016/j.msea.2005.03.008.
- [162] C. Ayas, V.S. Deshpande, N.A. Fleck, A fracture criterion for the notch strength of high strength steels in the presence of hydrogen, *J. Mech. Phys. Solids.* 63 (2014) 80–93. doi:10.1016/j.jmps.2013.10.002.
- [163] S. Pallaspuuro, H. Yu, A. Kisko, D. Porter, J. Kömi, Z. Zhang, Low-temperature hydrogen embrittlement in martensitic steels, in: *14th Int. Conf. Fract. (ICF 14)*, Rhodes, Greece, 2017: p. 2.
- [164] T. Depover, Evaluation of hydrogen embrittlement by mechanical testing, Ghent, 2011.
- [165] T. Depover, E. Wallaert, K. Verbeken, Fractographic analysis of the role of hydrogen diffusion on the hydrogen embrittlement susceptibility of DP steel, *Mater. Sci. Eng. A.* 649 (2016) 201–208. doi:10.1016/J.MSEA.2015.09.124.



## Original research articles

- I Pallaspuuro S, Linnell T, Suikkanen P, Porter D (2014)  $T_0 - T_{28J}$  correlation of low-carbon ultra-high-strength quenched steels, *Procedia Materials Science* 3: 1032-1037.
- II Wallin K, Pallaspuuro S, Valkonen I, Karjalainen-Roikonen P, Suikkanen P (2015) Fracture properties of high performance steels and their welds, *Engineering Fracture Mechanics* 135: 219-231.
- III Pallaspuuro S, Kaijalainen A, Mehtonen S, Kömi J, Zhang Z, Porter D (2018) Effect of microstructure on the impact toughness transition temperature of direct-quenched steels, *Materials Science and Engineering: A* 712: 671-680.
- IV Pallaspuuro S, Mehtonen S, Kömi J, Zhang Z, Porter D (2018) Effects of inclusions and local grain size on the low-temperature toughness of a low-carbon as-quenched steel, manuscript.
- V Pallaspuuro S, Yu H, Kisko A, Porter D, Zhang Z (2017) Fracture toughness of hydrogen charged as-quenched ultra-high-strength steels at low temperatures, *Materials Science and Engineering: A* 688: 190-201.

Papers I–III and V reprinted with permission from Elsevier.

Original research articles are not included in the electronic version of the dissertation.



639. Shashika Manosha Kapuruhamy Badalge, (2018) Convex optimization based resource allocation in multi-antenna systems
640. Koskela, Pekka (2018) Energy-efficient solutions for wireless sensor networks
641. Vuokila, Ari (2017) CFD modeling of auxiliary fuel injections in the blast furnace tuyere-raceway area
642. Vallivaara, Ilari (2018) Simultaneous localization and mapping using the indoor magnetic field
643. Kaparulina, Ekaterina (2018) Eurasian Arctic ice sheets in transitions : consequences for climate, environment and ocean circulation
644. Pramila, Anu (2018) Reading watermarks with a camera phone from printed images
645. Leppänen, Teemu (2018) Resource-oriented mobile agent and software framework for the Internet of Things
646. Klets, Olesya (2018) Subject-specific finite element modeling of the knee joint to study osteoarthritis development and progression
647. Shams Shafigh, Alireza (2018) New networking paradigms for future wireless networks
648. Mikhaylov, Konstantin (2018) Plug and play reconfigurable solutions for heterogeneous IoT
649. Verrollot, Jordan (2018) Mature supply management as an enabler for rapid product development and product portfolio renewal
650. Kemppainen, Anssi (2018) Adaptive methods for autonomous environmental modelling
651. Nyländén, Teemu (2018) Application specific programmable processors for reconfigurable self-powered devices
652. Asres, Georgies Alene (2018) Synthesis, characterization and application of WS<sub>2</sub> nanowire-nanoflake hybrid nanostructures
653. Hajimammadov, Rashad (2018) Plasmonic, electrical and catalytic properties of one-dimensional copper nanowires: Effect of native oxides
654. Barua, Bidushi (2018) Incentivizing user participation in cooperative content delivery for wireless networks

S E R I E S E D I T O R S

**A**  
**SCIENTIAE RERUM NATURALIUM**  
*University Lecturer Tuomo Glumoff*

**B**  
**HUMANIORA**  
*University Lecturer Santeri Palviainen*

**C**  
**TECHNICA**  
*Postdoctoral research fellow Sanna Taskila*

**D**  
**MEDICA**  
*Professor Olli Vuolteenaho*

**E**  
**SCIENTIAE RERUM SOCIALIUM**  
*University Lecturer Veli-Matti Ulvinen*

**E**  
**SCRIPTA ACADEMICA**  
*Planning Director Pertti Tikkanen*

**G**  
**OECONOMICA**  
*Professor Jari Juga*

**H**  
**ARCHITECTONICA**  
*University Lecturer Anu Soikkeli*

**EDITOR IN CHIEF**  
*Professor Olli Vuolteenaho*

**PUBLICATIONS EDITOR**  
*Publications Editor Kirsti Nurkkala*

ISBN 978-952-62-1896-0 (Paperback)  
ISBN 978-952-62-1897-7 (PDF)  
ISSN 0355-3213 (Print)  
ISSN 1796-2226 (Online)

